An intrinsic growth instability in isotropic materials leads to quasi-two-dimensional nanoplatelets

Andreas Riedinger[1†], Florian D. Ott[1†], Aniket Mule[1], Sergio Mazzotti[1], Philippe N. Knüsel[1], Stephan J. P. Kress[1], Ferry Prins[1], Steven C. Erwin[2*] and David J. Norris[1*]

[1]Optical Materials Engineering Laboratory, Department of Mechanical and Process Engineering, ETH Zurich, 8092 Zurich, Switzerland.
[2]Center for Computational Materials Science, Naval Research Laboratory, Washington, D.C. 20375 USA.

[†]These authors contributed equally to this work.
*email: steve.erwin@nrl.navy.mil; dnorris@ethz.ch

Supplementary information

Contents

Section 1. Modeling and theory

a. Diffusion-limited and surface-reaction-limited kinetics. Our model explains how surface-reaction rates can lead to nanoplatelets. However, in standard colloidal syntheses, CdSe nanocrystals typically grow as nearly spherical quantum dots. This seems to contradict the predictions of our model. Thus, the question arises why do some reaction conditions lead to quantum dots and some to NPLs for the same material.

We note that the selectivity leading to NPLs will only appear if the surface reactions are the rate-limiting steps in the overall growth process. To correctly describe crystal growth we must regard the overall incorporation reaction of a monomer from solution into a crystal surface as a two-step process: (i) Diffusion from the solution to the crystal surface i, is described by

$$\mathrm{r}_{\mathrm{diff},i} = -\mathrm{D}\frac{(\mathrm{c}_{\mathrm{surf},i}-\mathrm{c}_{\infty})}{\delta}\,, \tag{S1}$$

where D, δ, c_{∞}, and $\mathrm{c}_{\mathrm{surf},i}$ are the diffusion coefficient in solution, the diffusion-layer thickness, the monomer concentration far away from the surface, and the monomer concentration at the surface, respectively. (ii) Incorporation of the monomer into the surface i, which we treat as a general n-th order reaction, is described by

$$\mathrm{r}_{\mathrm{surf},i} = \mathrm{c}_{\mathrm{surf},i}^{n}\mathrm{k}_{\mathrm{surf},i}\,, \tag{S2}$$

where $\mathrm{k}_{\mathrm{surf},i}$ is the surface-reaction constant.

Under steady-state conditions the two rates $\mathrm{r}_{\mathrm{diff}}$ and $\mathrm{r}_{\mathrm{surf}}$ must be equal:

$$\mathrm{r}_{i} = \mathrm{c}_{\mathrm{surf},i}^{n}\mathrm{k}_{\mathrm{surf},i} = -\mathrm{D}\frac{(\mathrm{c}_{\mathrm{surf},i}-\mathrm{c}_{\infty})}{\delta}\,, \tag{S3}$$

$$\frac{(\mathrm{c}_{\infty}-\mathrm{c}_{\mathrm{surf},i})}{\mathrm{c}_{\mathrm{surf},i}^{n}} = \frac{\mathrm{k}_{\mathrm{surf},i}}{\mathrm{D}/\delta}\,. \tag{S4}$$

If the reaction is diffusion-limited then $\mathrm{k}_{\mathrm{surf},i} \gg \mathrm{D}/\delta$, meaning that $\mathrm{c}_{\mathrm{surf},i} \ll \mathrm{c}_{\infty}$. Consequently, the growth rates for all surfaces are approximately given by $\mathrm{D}\frac{\mathrm{c}_{\infty}}{\delta}$ and no selectivity will be observed. In this diffusion-limited case, the obtained crystals will have a

nearly spherical shape because diffusion in liquids is usually isotropic. This is the condition under which we can expect quantum dots.

On the other hand, if the overall reaction is limited by the surface incorporation, we find: $\mathrm{k_{surf,}}_i \ll \mathrm{D}/\delta$, resulting in a surface concentration given by $\mathrm{c_{surf,}}_i \approx \mathrm{c}_\infty$. Then the reaction rate for facet i is given by:

$$\mathrm{r}_i = \mathrm{c}_\infty^n \mathrm{k_{surf,}}_i \ . \qquad \text{(S5)}$$

In this surface-reaction-limited case, clear selectivity would result. A larger surface-reaction constant $\mathrm{k_{surf,}}_i$ will lead to faster growth. This is the limit under which we expect the growth of nanoplatelets.

b. Model of two-dimensional nucleation and growth of nanoplatelets. Here we provide further details about our evaluation of the nucleation barriers to form islands on surfaces. We assume that the change in energy upon island nucleation depends on the change in total crystal volume (ΔV), surface area (ΔA), and edge length (ΔL):

$$\Delta E = E_V \Delta V + E_A \Delta A + E_L \Delta L \ . \qquad \text{(S6)}$$

Here, E_V, E_A, and E_L are respectively volume, surface, and line energies. E_V is the energy difference in chemical potential of CdSe between the crystalline phase and the melt per unit volume of a CdSe monomer in the zincblende bulk crystal phase; thus E_V is the thermodynamic driving force for crystallization. E_A is the surface formation energy of Cd-rich CdSe(001) passivated by acetate ions. From DFT calculations (see Supplementary Section 1.c) we obtained E_A = 5.7 meV/Å^2 under Se-rich conditions. E_L is the edge formation energy of a monolayer-high step on Cd(001); from DFT we obtained 37.1 meV/Å. We consider only monolayer islands, for which the height (L_1) is half the lattice parameter of the unit cell (a_0), *i.e.* $L_1 = \frac{a_0}{2} = 3.10$ Å. Hence, the additional volume ΔV for an island is equal to the projected area, a, of the island times the island height: $\Delta \mathrm{V} =$

$L_1 a$. Similarly, the additional surface area ΔA is equal to the projected perimeter of the island (L_{island}) times the island height: $\Delta A = L_1 L_{\text{island}}$. The evaluation of the total added edge length is slightly more complex. As can be seen from Fig. 3a in the main text, the increase in total edge length arises from the part of the island perimeter forming a step with length L_{step}, plus 4 edges with length L_1: $\Delta L = L_{\text{step}} + 4L_1$. We substitute these expressions into Eq. (S6) and obtain for the island formation energy:

$$\Delta E\left(a, L_{\text{island}}, L_{\text{step}}\right) = (L_1 E_V)a + L_1 E_A L_{\text{island}} + E_L\left(L_{\text{step}} + 4L_1\right) . \quad \text{(S7)}$$

The shape of a growing island evolves so as to minimize its formation energy at every point along a generalized reaction coordinate, which we take to be the projected area, *a*, of the island:

$$\mathrm{d}\Delta E|_a = 0 . \quad \text{(S8)}$$

The solution of Eq. (S8) describes the minimum energy path for the formation reaction of a stable island. The maximum of this curve, if it exists, corresponds to the nucleation barrier, $\Delta E^{\text{barrier}}$. We evaluate the formation energy of the most stable island with a given area and underlying surface shape under our assumption that the crystallite is bounded by {001} facets. We find that the solution of Eq. (S8) depends on the facet dimensions. On wide facets, for which the characteristic size of the island is smaller than the facet thickness, we assume for simplicity a rectangular island originating from a corner of the facet (see Fig. 3a in the main text). The formation energy is minimized for a square island of edge length, $\sqrt{a}$, leading to:

$$E^{\text{wide}}(a) = L_1 E_V a + 4L_1\sqrt{a}E_A + 2\left(\sqrt{a} + 2L_1\right)E_L , \quad \text{(S9)}$$

$$= L_1 E_V a + (4L_1 E_A + 2E_L)\sqrt{a} + 4L_1 E_L . \quad \text{(S10)}$$

For sufficiently large islands on narrow facets, the most stable island has a rectangular shape covering the full width of the facet (see Fig. 3a in the main text). In this regime the island formation energy is

$$E^{\text{narrow}}(a) = L_1 E_V a + \left(2mL_1 + \frac{2a}{mL_1}\right) L_1 E_A + (m+4) L_1 E_L \ , \tag{S11}$$

$$= \left(L_1 E_V + \frac{2E_A}{m}\right) a + 2mL_1^2 E_A + (m+4) L_1 E_L \ . \tag{S12}$$

These solutions are shown in Fig. 3b in the main text for a range of different facet widths (*i.e.*, thicknesses) *m*.

c. Evaluation of surface, edge, and volume energies. The surface and edge energies, E_A and E_L, on CdSe(001) are formation energies defined with respect to a reference system (here the reservoirs of different chemical species),[S1,S2,S3]

$$\Delta H_f(X) = E_{\text{tot}}^{\text{DFT}}(X) - \sum_i n_i \mu_i \ . \tag{S13}$$

E_A and E_L are per unit surface area and per unit step length, respectively. We use the superscript "DFT" for values directly taken from a single DFT total-energy calculation. X is the system including the defect (a surface or a step). The sum in Eq. (S13) accounts for the fact that each element i, contained n_i times in X, has a chemical potential, μ_i.

The NPLs, surfaces, and edges are comprised of Cd, Se, and the surfactant acetate molecules, (AcO, $H_3C_2O_2$), which we consider to be indivisible. Following standard practice, we assumed thermodynamic equilibrium between CdSe and reservoirs of Cd and Se. Thus, we have:

$$(\mu_{\text{Cd}} + \mu_{\text{Se}}) = E_{\text{CdSe}}^{\text{DFT}} \ . \tag{S14}$$

The analogous assumption for $Cd(AcO)_2$ gives:

$$\mu_{\text{Cd}} + 2\mu_{\text{AcO}} = E_{\text{Cd(AcO)}_2}^{\text{DFT}} \ . \tag{S15}$$

Due to the presence of elemental selenium in the reaction we also assumed, for concreteness, that the experiments were conducted under Se-rich conditions:

$$\mu_{\text{Se}} = E_{\text{Se,bulk}}^{\text{DFT}} \ . \tag{S16}$$

These three conditions fix the values of the three chemical potentials. For the bulk phases we used the relaxed structures of zincblende CdSe ($E_{\mathrm{CdSe}}^{\mathrm{DFT}}$), γ-Se ($E_{\mathrm{Se,bulk}}^{\mathrm{DFT}}$), and a 2-dimensional coordination polymer of Cd acetate [$E_{\mathrm{Cd(OAc)_2}}^{\mathrm{DFT}}$, see Supplementary Fig. 14].

To calculate the surface energy E_A we used a 4-monolayer-thick CdSe slab in vacuum with Cd-terminated {001} surfaces on both sides passivated with acetate ions (see Supplementary Fig. 15). We obtained $E_A = 5.7\ \frac{\mathrm{meV}}{\mathrm{Å}^2}$, the value used in the main text. As expected, this value is much lower than typical surface energies for unpassivated surfaces.

To define the edge energy E_L we used three islands of different width (Supplementary Fig. 16b-d) and took the average as a single representative value appropriate for small islands. This average is $E_L = 37\ \frac{\mathrm{meV}}{\mathrm{Å}}$, the value used in the main text. We caution that the high and low values (47 and 24 meV/Å) are quite different from this average, and hence the results should be understood as trends rather than precise values.

Finally, we turn to the volume energy E_V. Crystals form from supersaturated melts or solutions because a thermodynamic driving force exists for a monomer in the solution/melt to incorporate into the crystal. In our model the energy gain per monomer incorporated into a bulk crystal is given by $V_m E_V$, where V_m is the volume of a monomer in bulk CdSe. While E_A and E_L can be estimated from DFT calculations for well-defined structures, this is less straightforward for E_V because the melt is difficult to model. Thus, instead of DFT, we used experimental observations to estimate the value of E_V.

From the experimental absence of CdSe nanoplatelets with thicknesses above 5 monolayers we conclude that for the related surface widths ($m > 5$) no kinetic instabilities exist. Accordingly, the critical-sized wide-facet island will form before the narrow-facet regime is reached. We assumed that for the thinnest non-existing population

with a thickness of 6 monolayers the narrow-facet regime starts exactly when the island area coincides with that of the critical-sized wide-facet island:

$$\Delta E_6^{\text{barrier}} = \Delta E_{\text{wide}}^{\text{barrier}} \ . \tag{S17}$$

From the solution of Eq. (S17) we find $E_V = -2.2\ \frac{\text{meV}}{\text{Å}^3}$, which is the value we used to evaluate our results shown in Fig. 3b.

The computations as described above for CdSe were repeated for CdS and CdTe. The results are summarized in Supplementary Table 1.

Supplementary Table 1. Energy parameters for CdS, CdSe, and CdTe

Material	$E_V\ \left(\frac{\text{meV}}{\text{Å}^3}\right)$	$E_A\ \left(\frac{\text{meV}}{\text{Å}^2}\right)$	$E_L\ \left(\frac{\text{meV}}{\text{Å}}\right)$	$m_{\text{max}} + 1$
CdS	$\mathbf{-4.2}$	$\mathbf{8.4}$	$\mathbf{76}$	$\mathbf{6}$
CdSe	$\mathbf{-2.2}$	$\mathbf{5.7}$	$\mathbf{37}$	$\mathbf{6}$
CdTe	$\mathbf{-0.7}$	$\mathbf{1.1}$	$\mathbf{26}$	$\mathbf{9}$

$\boldsymbol{m}_{\text{max}}$: Maximum observed nanoplatelet thickness in monolayers.

d. Simple kinetic model of reversible crystal growth. The nucleation model presented in Supplementary Section 1.b explains why growth is faster on thin facets, assuming an overall driving force for growth exists. However, it does not take into account the reversibility of the growth or the fact that thermodynamic driving forces may change throughout the reaction, for example, by the decaying supersaturation of reactants. To address this, we developed a simple kinetic model to describe the temporal evolution of five different populations: free monomers (N_0) and monomers embedded in NPLs with thicknesses from 2 to 5 monolayers (N_{2-5}). NPLs thinner than 2 monolayers are not stable, and under the given reaction conditions, no kinetic growth instability exists for thicker ones.

To begin, we constrain our system by the mass conservation law:

$$\sum_m N_m(t) = N_{\mathrm{tot}} \ . \tag{S18}$$

We describe attachment and detachment reactions of monomers on the crystal surfaces as first-order processes. This means that we assume that on a nanoplatelet ($m = 2, 3, 4, 5$) the attachment rate is proportional to the free-monomer concentration and the detachment rate is proportional to the bound-monomer concentration:

$$\frac{\mathrm{d}N_m(t)}{\mathrm{d}t} = k_m N_0(t) - k_{-m} N_m(t) \ , \tag{S19}$$

where k_m and k_{-m} are the rate constants for attachment and detachment, respectively. Based on (S18) and (S19) we can also express $N_0(t)$ in its derivative form:

$$\frac{\mathrm{d}N_0(t)}{\mathrm{d}t} = -N_0(t) \sum_{m\neq 0} k_m + \sum_{m\neq 0} k_{-m} N_m(t) \ . \tag{S20}$$

This set of differential equations in matrix notation is ($\sum_{m\neq 0} k_m = k_{\mathrm{tot}}$):

$$\frac{\mathrm{d}}{\mathrm{d}t}\begin{pmatrix} N_0(t) \\ N_2(t) \\ N_3(t) \\ N_4(t) \\ N_5(t) \end{pmatrix} = \begin{pmatrix} -k_{\mathrm{tot}} & k_{-2} & k_{-3} & k_{-4} & k_{-5} \\ k_2 & -k_{-2} & 0 & 0 & 0 \\ k_3 & 0 & -k_{-3} & 0 & 0 \\ k_4 & 0 & 0 & -k_{-4} & 0 \\ k_5 & 0 & 0 & 0 & -k_{-5} \end{pmatrix} \begin{pmatrix} N_0(t) \\ N_2(t) \\ N_3(t) \\ N_4(t) \\ N_5(t) \end{pmatrix} , \tag{S21}$$

or written in compact form:

$$\frac{\mathrm{d}}{\mathrm{d}t}\boldsymbol{x}(t) = \mathbf{K}\boldsymbol{x}(t) \ . \tag{S22}$$

This problem can be diagonalized using the unitary matrix $\mathbf{U}$ which contains column-wise the eigenvectors of $\mathbf{K}$:

$$\frac{\mathrm{d}}{\mathrm{d}t}[\mathbf{U}^{-1}\boldsymbol{x}(t)] = (\mathbf{U}^{-1}\mathbf{K}\mathbf{U})[\mathbf{U}^{-1}\boldsymbol{x}(t)] \ , \tag{S23}$$

$$\frac{\mathrm{d}}{\mathrm{d}t}\tilde{\boldsymbol{x}}(t) = \boldsymbol{\lambda}\tilde{\boldsymbol{x}}(t) \ , \tag{S24}$$

where $\tilde{\boldsymbol{x}}(t) = \mathbf{U}^{-1}\boldsymbol{x}(t)$ and $\boldsymbol{\lambda} = \mathbf{U}^{-1}\mathbf{K}\mathbf{U}$ is a diagonal matrix containing the eigenvalues of $\mathbf{K}$. Having uncoupled the set of differential equations they can be solved separately:

$$\frac{\mathrm{d}}{\mathrm{d}t}\tilde{x}_i(t) = \lambda_{ii}\tilde{x}_i(t) \ , \tag{S25}$$

$$\tilde{x}_i(t) = \tilde{x}_i(0)e^{\lambda_{ii}t} \ . \tag{S26}$$

To find the values $\tilde{x}_i(0)$ we need to evaluate the coordinate transformation at $t = 0$ for which we know that all monomers (N_{tot}) are in their free form:

$$\tilde{\boldsymbol{x}}(0) = \mathbf{U}^{-1}\boldsymbol{x}(0) = \mathbf{U}^{-1}(N_{\mathrm{tot}}, 0,0,0,0)^T \ . \tag{S27}$$

Finally, we obtain the solution by reversing the transformation from above:

$$\boldsymbol{x}(t) = \mathbf{U}\tilde{\boldsymbol{x}}(t) \ . \tag{S28}$$

We next need to evaluate k_m and k_{-m}. Monomer attachment and detachment occur on kink sites along surface steps at the edges of islands[S4,S5,S6]. The number of such islands is proportional to the rate at which they are nucleated, *i.e.*, $\exp\left(-\frac{\Delta E_m^{\mathrm{barrier}}}{\mathrm{kT}}\right)$, where $\Delta E_m^{\mathrm{barrier}}$ is the island nucleation barrier, k is the Boltzmann constant, and T is absolute temperature. The rates of monomer attachment and detachment are proportional to the island number and the facet thickness *m*:

$$k_m = C_0 m \exp\left(-\frac{\Delta E_m^{\mathrm{barrier}}}{\mathrm{kT}}\right), \tag{S29}$$

$$k_{-m} = C_0 m \exp\left(-\frac{\Delta E_m^{\mathrm{barrier}}}{\mathrm{kT}}\right) A_m \ . \tag{S30}$$

The prefactor C_0 includes all terms in the rate constant that are assumed to be equal for the various reactions, and A_m accounts for the additional energy penalty to detach a monomer from its bound state in the nanoplatelet, making the detachment reaction slower. Since the ratio k_m/k_{-m} is equal to the equilibrium constant, we find for A_m:

$$A_m = \frac{k_{-m}}{k_m} = \exp\left(\frac{\Delta H_{f,m}}{kT}\right) = \exp\left(\frac{2L_1^3 E_V + \frac{4L_1^2}{m} E_A}{kT}\right), \tag{S31}$$

with $\Delta H_{f,m}$ being the reaction energy per monomer in the limit of large platelets.

The remaining free parameter, C_0, was used to fit the solution of this set of ordinary differential equations to the experimentally recorded absorption spectra (Fig. 2a in the main text) of 2- and 3-monolayer-thick NPLs (the absorption data were normalized to the

total amount of CdSe absorption at 350 nm). We obtained a general attempt frequency of $C_0 = 2.7\times10^9\ \mathrm{Hz}$. The resulting dynamics of the different populations are shown in Supplementary Fig. 17a and Fig. 2b in the main text.

We now consider our assumption of first-order kinetics for monomer incorporation and dissolution. Derivations of explicit nucleation rates reveal second-order kinetics[S7] and the rate of dissolution is proportional to the amount of exposed monomers on the reactive surface rather than to the total amount of monomers in the NPLs. Since the reactive surface involves the few-monolayer-thick side facets, its area is proportional to $N_m^{1/2}(t)$. These considerations lead to kinetics very different from first order:

$$\frac{\mathrm{d}N_m(t)}{\mathrm{d}t} = k_m N_0^2(t) - k_{-m} N_m^{1/2}(t)\ . \tag{S32}$$

In Supplementary Fig. 17, we show a comparison of numerical solutions for our first-order-kinetics model and the more advanced model based on the same set of reaction constants, k_m and k_{-m}. We can clearly observe the same qualitative behavior in both cases. In the more realistic model, the equilibrium conditions have changed due to the reaction order:

$$K_m = \exp\left(-\frac{2L_1^3 E_V + \frac{4L_1^2}{m} E_A}{kT}\right) = \frac{N_{m,\mathrm{eq}}^{1/2}}{N_{0,\mathrm{eq}}^2}\ , \tag{S33}$$

which leads to an equilibrium ratio between populations i and j that is squared compared to the first-order model:

$$\frac{N_{i,\mathrm{eq}}}{N_{j,\mathrm{eq}}} = \frac{K_i^2}{K_j^2}\ . \tag{S34}$$

The important point is that the simplified first-order model predicts the same qualitative behavior as the higher-order model. The former only slightly underestimates the selectivity of the synthesis.

e. Calculation of the surfactant desorption barriers. We evaluated the activation barriers for desorption of the surfactants from the NPL surface to better understand where CdSe monomers are most likely to adsorb during growth. We found that monomers preferentially adsorb near steps, which is consistent with the growth model described in the main text.

To evaluate the barrier for an acetate (or Cd acetate) to desorb from the CdSe surface we determined the minimum-energy reaction path using the nudged-elastic-band (NEB) method as implemented in VASP[S8]. We used 9 NEB images between the two endpoints of the reaction coordinates; this identifies the transition state with sufficient accuracy for our purposes. The specific reactions we investigated included: (i) acetate desorption from a flat surface, (ii) Cd acetate desorption from a flat surface, and (iii) acetate desorption from a step. Initial and final structures and the corresponding minimum energy paths of these reactions are shown in Supplementary Fig. 18.

f. Kinetic Monte Carlo simulations of nanoplatelet growth. Atomistic simulations provide an independent way to validate our explanation of the instability that leads to NPLs. We thus applied the kinetic Monte Carlo (kMC) method to NPL growth. We considered only adsorption and desorption of monomers, but not their diffusion (either on the surface of the nanocrystal or in solution). We treated monomer adsorption and desorption as thermally activated processes with Arrhenius-type reaction rates. In the real system, the adsorption of a CdSe monomer requires three separate steps: (i) desorption of a surfactant molecule to expose a surface site, (ii) adsorption of a monomer onto that site, and (iii) re-adsorption of a surfactant molecule to maintain the passivated surface. Of these three steps only the first has an energy barrier. Therefore, the *effective* barrier for adding a monomer to a surface site $\Delta E_{\mathrm{ads}}^{\mathrm{barrier}}$ is given by the barrier for desorbing a surfactant molecule. We obtained these barriers from DFT/NEB calculations as discussed in the

previous section. The results showed a strong preference of monomer adsorption on a step edge ($\Delta E_{\mathrm{ads}}^{\mathrm{barrier}} = 1.2\ \mathrm{eV}$) compared to a flat crystal surface ($\Delta E_{\mathrm{ads}}^{\mathrm{barrier}} = 2.1\ \mathrm{eV}$).

The desorption of a CdSe monomer also requires three steps: (i) desorption of the surfactant molecule, (ii) desorption of a monomer molecule, and (iii) re-adsorption of a surfactant. Two of these steps have a barrier, namely desorption of the surfactant and of the monomer. Compared to surfactants, monomers have a local environment which is much more variable – with 6 nearest-neighbor sites already in a simple cubic structure – leading to a large number of distinct scenarios. Instead of investigating each of these scenarios by DFT, we used a simplified model to estimate these site-dependent desorption barriers. First, we assumed that monomer and surfactant desorb together as a complex. Furthermore, we assumed that the transition state of this reaction is reached when the monomer and surfactant have broken their bond to the surface, but no surfactant has yet adsorbed at the open site left behind. As a consequence (see the schematic potential-energy surface in Supplementary Fig. 19), the barrier for monomer desorption can be easily estimated from the barrier for adsorption if the energy difference ΔE_{des} between the two endpoints of the reaction is also known. Thus we have:

$$\Delta E_{\mathrm{des}}^{\mathrm{barrier}} = \Delta E_{\mathrm{ads}}^{\mathrm{barrier}} + \Delta E_{\mathrm{des}} \ . \qquad \text{(S35)}$$

It is straightforward to evaluate the energy difference ΔE_{des} for any given local environment of a monomer. To do this, we used a modified bond-counting model based on a lattice of monomers. This model gives desorption barriers ranging from 0.1 eV for a single monomer sitting on a corner of a flat surface to 2.3 eV for a monomer incorporated in a flat surface. Each monomer in the nanocrystal makes n_B bonds (from 1 to 6) to its nearest neighbors. When a monomer is removed from the nanocrystal these bonds are broken and the monomer is considered "dissolved" in the melt (or solvent). Hence, desorption raises the energy of the system by $n_B \varepsilon_B$ and lowers it by $|\mu|$, where $\mu < 0$ is the chemical potential of

the dissolved monomer. We modified this standard bond-counting model by including an additional term arising from the energy per unit length E_L of the exposed edges of the nanocrystal; this parameter has the same value as in the main text, $E_L = 37\ \frac{\mathrm{meV}}{\text{Å}}$. Hence the energy change upon monomer desorption is

$$\Delta E_{\mathrm{des}} = n_B \varepsilon_B + \mu + E_L \Delta L \ . \tag{S36}$$

Finally, from expression (S36) follows a standard Arrhenius relationship between r_{des} and r_{ads}[S4,S5,S6]:

$$r_{\mathrm{des}} = r_{\mathrm{ads}} \exp\left(-\frac{\Delta E_{\mathrm{des}}}{kT}\right) . \tag{S37}$$

We now show that by enforcing the equivalence of the discrete expression (S36) with our continuum model (in the main text) for the energy of a nanocrystal, we can obtain the parameters ε_B and μ from the continuum parameters E_V and E_A.

To do this, we equate the two different expressions for the energy of a general crystallite built from monomer cubes with volume V_m. We begin with the continuum description. We group the monomers comprising the crystallite according to the number of their nearest neighbors: n_1 monomers with one nearest neighbor, n_2 monomers with two nearest neighbors, *etc*. Monomers with fewer than six nearest neighbors lead to a monomer face being exposed at the crystallite surface. Hence, a monomer with j nearest neighbors has $(6-j)$ exposed square surfaces, each with area $V_m^{2/3}$. Accordingly, the total energy is

$$E_{\mathrm{continuum}} = \sum_{i=1}^{6} n_i \left[V_m E_V + (6-i) V_m^{2/3} E_A\right] + E_L L \ , \tag{S38}$$

where L is the total edge length of the crystallite.

We now make the same evaluation using the discrete expression (S36). Each monomer in the crystallite must first be obtained from the melt and hence costs energy μ. In the crystallite, a monomer shares its bond with its i nearest neighbors. Thus, the total energy is

$$E_{\text{discrete}} = \sum_{i=1}^{6} n_i \left[-\frac{i}{2}\varepsilon_B - \mu \right] + E_L\, L \ . \tag{S39}$$

In order for the expressions (S38) and (S39) to be equal for arbitrary choices of $\{n_i\}$ we must have

$$-\frac{i}{2}\varepsilon_B - \mu = V_m E_V + (6-i) V_m^{2/3} E_A \ , \tag{S40}$$

which immediately yields the parameters ε_B and μ in terms of E_V and E_A:

$$\varepsilon_B = 2V_m^{2/3} E_S = 173 \text{ meV} \ , \tag{S41}$$

$$\mu = -V_m E_V - 6V_m^{2/3} E_S = -428 \text{ meV} \ . \tag{S42}$$

We started our simulations from small random crystallite nuclei containing 1 to 8 monomers. These are depicted at the top of Fig. 4 in the main text. At the actual experimental temperatures around 500 K the growth is extremely slow. This is because overgrowing a facet with a new layer starts with a sequence of highly unfavorable attachment steps. For example, the formation of a stable island on a 3-monolayer-wide facet along the minimum energy path requires a sequence of 5 very rare attachment steps with probabilities on the order of 10^{-11}, 10^{-2}, 10^{-1}, and 10^{-4}, respectively. Thus, to increase computational efficiency we ran the simulations at 650 K, we blocked monomer attachment on flat surfaces due to low reactivity (see surfactant desorption barriers), and we increased the sticking probability of single monomers to avoid repeated detachment and attachment steps.

A typical growth sequence is shown in Supplementary Movie 1 and a statistical summary of the results from 1000 simulation runs is shown in Fig. 4 in the main text. By increasing the temperature even further, for example to 1500 K, we observed that the selective growth of narrow facets is completely suppressed, and the crystallites grow isotropically (see Supplementary Movie 2). These results are consistent with the 2D nucleation model presented in the main text.

Due to the high step energy of growing islands, the crystal facets in our simulations are almost perfectly flat: an island either quickly re-dissolves or overgrows the complete facet. Therefore, we can conveniently describe these crystals by the three side lengths of a rectangular box. We use the largest box spanned by the lattice points containing no unoccupied sites. We define the shortest side length as the thickness. Then the characteristic side length of the nanoplatelet is given by the square root of the maximum projected area of the box. In Fig. 4 in the main text we plot the thickness versus characteristic side length for a set of nanocrystals obtained from simulations starting with small crystal nuclei of various shapes. We observe two types of growth: (i) crystals that reach an increased thickness at early stages in the simulations and grow equally slowly in all directions, forming isotropic crystallites; (ii) crystals that remain thin while growing faster in the other two lateral dimensions, forming extended flat nanoplatelets.

To quantify these observations we assign each nanocrystal obtained from our simulations to one of the growth types from above, based on the aspect ratio between its characteristic side length and thickness. If this aspect ratio is larger than two, the nanocrystal evolved under type-(ii) growth obtaining quasi-two-dimensional shapes. Otherwise, the simulation outcome is better described by type-(i) growth. In total, 94.9% of all simulation runs evolved under the type-(ii)-growth mode. For 2- and 3-monolayer-thick nanocrystals, the fraction of type-(ii) growth was at 100% and 93.4%, respectively. Thicker nanocrystals did not yield strongly anisotropic shapes [only 0.1 % and 0.0 % of 4- and 5-monolayer-thick nanocrystals grew under the type-(ii)-growth mode, respectively]. This is due to their physically (and also computationally) much slower lateral growth rates.

Thus, these kMC simulations give insight into the microscopic mechanism of nanoplatelet growth. Using the simple concepts of nearest-neighbor binding and a penalty for forming edges, these atomistic simulations confirm our 2-dimensional nucleation and growth

model. We anticipate that this method will allow us to further explore the parameter space controlling nanoplatelet growth and to investigate its behavior on extended time scales.

g. Evaluation of the model parameters for cubic FeS_2. To explore the ability of our model to predict new nanoplatelet materials we investigated crystal growth for cubic FeS_2 (pyrite). These crystals have relatively stable (001) surfaces even when unpassivated[S9]. According to our model, such stability is favorable for platelet growth. We therefore applied DFT to estimate the model parameters E_A and E_L (see Supplementary Section 1.c and Supplementary Fig. 20). To account for the magnetization of pyrite surfaces[S9] we included spin-polarization in our calculations.

For the surface and edge energies we obtained values of $E_A = 64$ meV/Å^2 and $E_L = 47$ meV/Å, respectively. These results show that a considerable fraction of the step-formation energy during island growth is due to the edge energy:

$$\frac{E_L}{E_L + L_1 E_A} \approx 21\% \,. \qquad \text{(S43)}$$

This edge contribution disappears wherever the island has reached the boundary of the underlying surface facet explaining why crystal growth on wide facets can have higher energy barriers than on narrow facets (see Fig. 3a in the main text). Based on these results we conclude that under appropriate experimental conditions, in the absence of diffusion-limitations, the formation of FeS_2 nanoplatelets could be possible.

This prediction was then tested via colloidal synthesis (see Methods). Our results show that indeed NPLs are formed (see Supplementary Fig. 13). The obtained platelets have the cubic crystal structure and a stoichiometry of FeS_2 (*i.e.* pyrite). Our data are also consistent with a thickness of two monolayers. Moreover, by varying the growth conditions (*e.g.* temperature and concentration), we were unable to synthesize thinner or thicker pyrite NPLs. From the absence of 3-monolayer-thick nanoplatelets we then estimated that

the formation energy of pyrite per unit volume is $E_V = 24$ meV/Å^3 under our experimental conditions (see Supplementary Section 1.c).

Supplementary Fig. 21 shows the resulting energy paths during crystal growth on 1-monolayer-thick, 2-monolayer-thick, and wide facets. We see that under these conditions only a single instability exists for the 2-monolayer-thick nanoplatelets. Monolayer sheets are not stable because their surface-to-volume ratio is too large, leading to a positive slope of the energy curve during narrow-facet growth. The activation energy for growth on a 2-monolayer-thick facet is 0.26 eV lower than on a wide facet. This implies that lateral growth is three orders of magnitude faster than growth in the thickness direction under our experimental reaction temperatures.

Therefore, we have successfully applied the concepts of our model to obtain NPLs of cubic FeS_2, a new material system. From our DFT study we could conclude that this material has suitable surface properties—low surface energy and high step energy—to grow anisotropically as a quasi-2-dimensional material. This was then experimentally confirmed.

Section 2. Supplementary figures

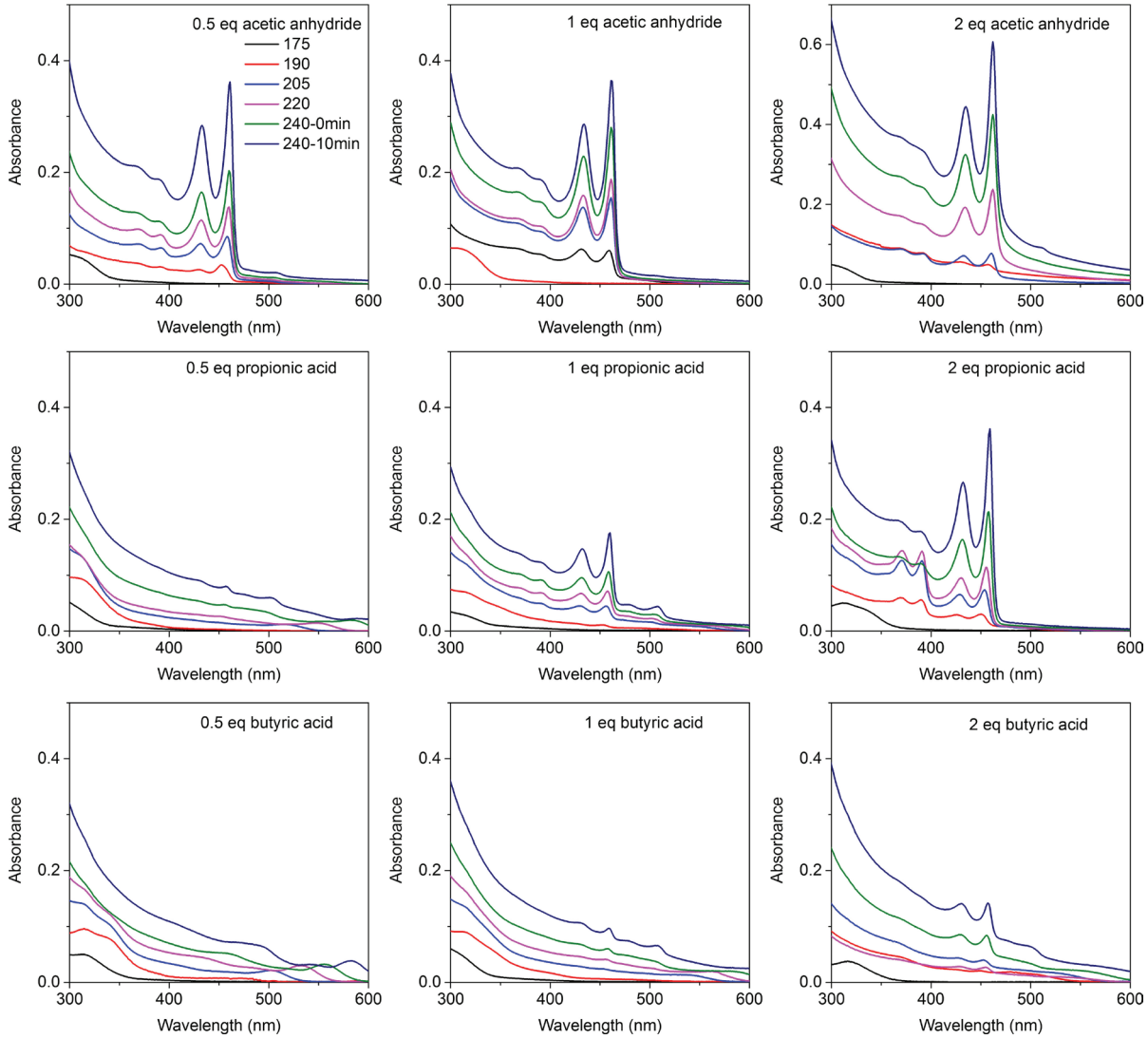

Supplementary Figure 1 | Absorption spectra taken during NPL syntheses with acetic anhydride, propionic acid, and butyric acid. Spectra of the aliquots collected during the course of the reaction were recorded without further dilution or purification. The dilution factor was the same for all aliquots and syntheses, hence differences in absorbance between samples are absolute and thus directly comparable. A clear trend was observed: the longer the aliphatic chain of the carboxylic acids, the higher their required concentration for efficient NPL formation. The injection of acetic anhydride yielded NPLs even at 0.5 equivalents (eq), propionic acid around 1 eq, and butyric acid yielded few NPLs even at 2 eqs. When 2 eq acetic anhydride were injected, significant scattering was observed. Interestingly, only with 2 eq propionic acid, clear absorption features of 2-monolayer-thick NPLs (371 and 391 nm) were observed at early time points, which diminished over the course of the reaction while absorption intensities of 3-monolayer-thick NPLs (432 and 458 nm) increased and were dominant at the end of the reaction.

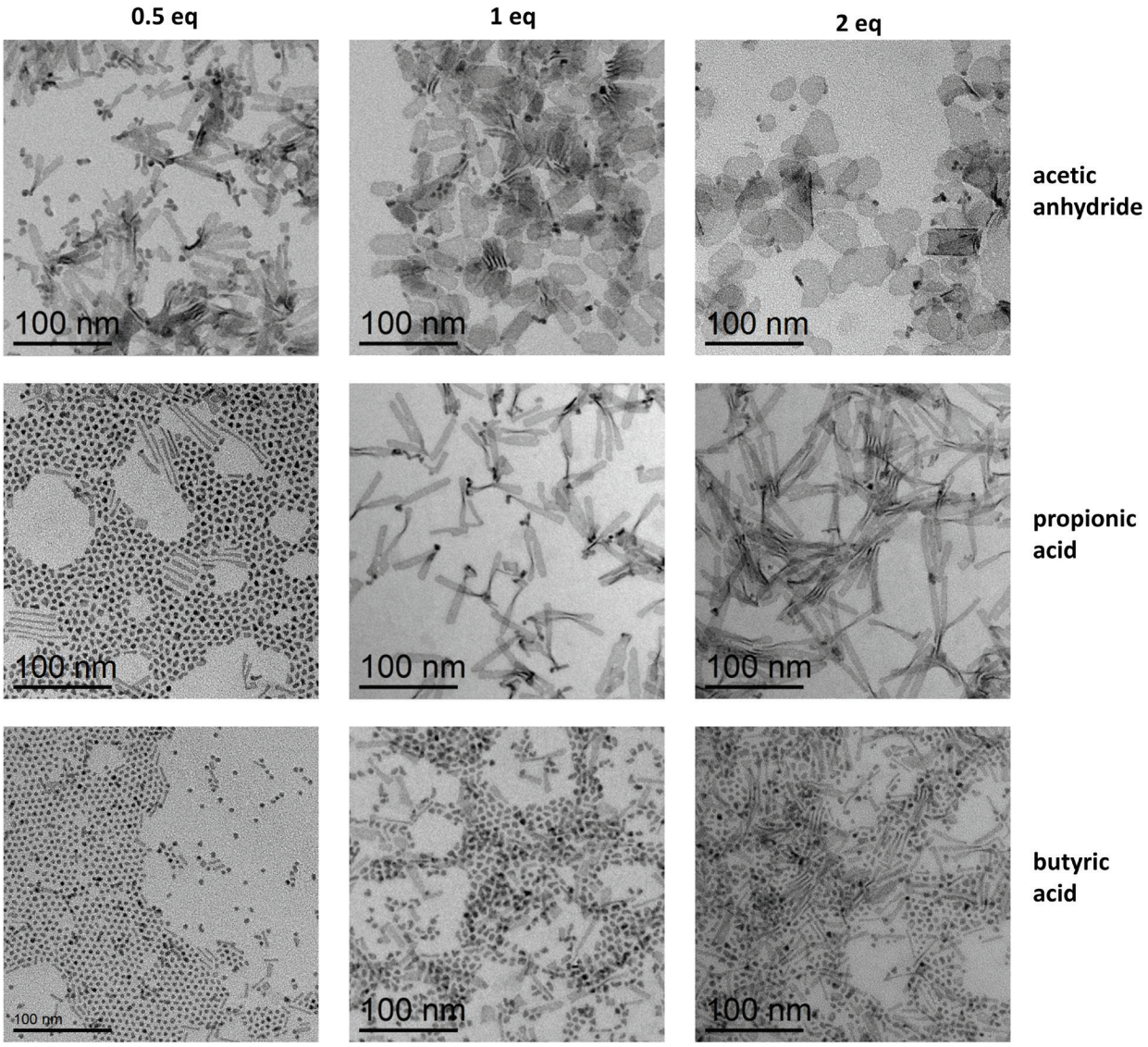

Supplementary Figure 2 | TEM micrographs of the reaction products obtained with 0.5 to 2 equivalents (eq) acetic anhydride, propionic acid, and butyric acid. Lateral dimensions of NPLs increased with acetic anhydride concentration, while the aspect ratio decreased, and more irregularly shaped NPLs were formed with 2 eq. 0.5 eq propionic acid yielded mainly quasi-zero-dimensional nanocrystals (quantum dots) and only a few NPLs with high aspect ratio were observed, which did not change as the concentration of propionic acid was increased (even though lateral dimension increased). The addition of butyric acid yielded only a few NPLs at all tested concentrations. At the highest concentration of butyric acid, more irregularly shaped nanocrystals were observed.

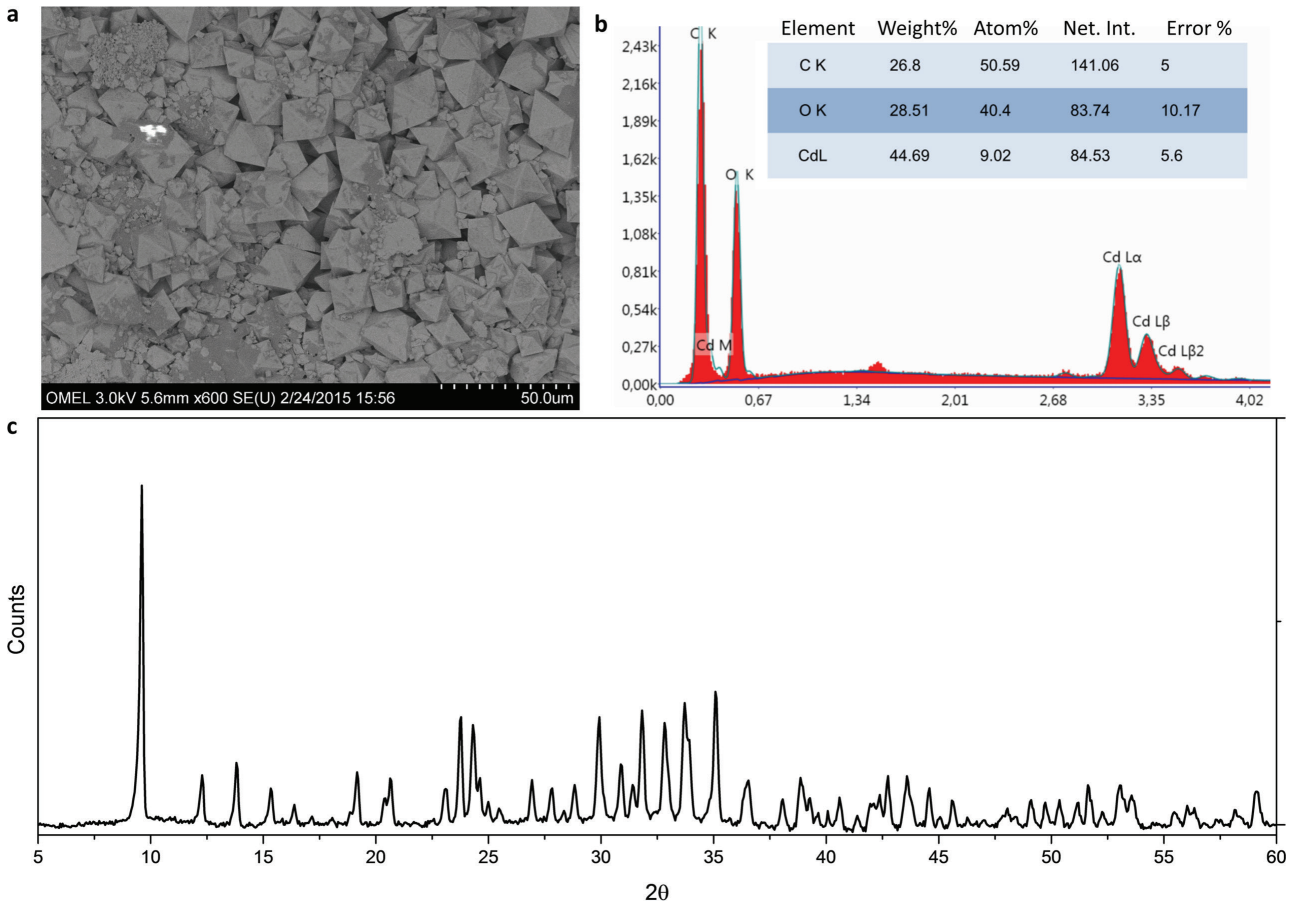

Supplementary Figure 3 | Analysis of the product obtained when acetic anhydride is added to Cd(oleate)$_2$ in absence of Se. a, Scanning electron micrographs (SEMs) revealed that large crystals were formed. **b**, The chemical composition was found to be very close to pure Cd(acetate)$_2$ by energy-dispersive X-ray spectroscopy (EDS) analysis (obtained at 10 kV, x-axis in keV and y-axis in counts). The slightly higher carbon content possibly stems from oleate impurities. **c**, The corresponding powder X-ray diffraction (XRD) pattern exhibited very sharp peaks. This phase could not be indexed with reasonable fit factors.

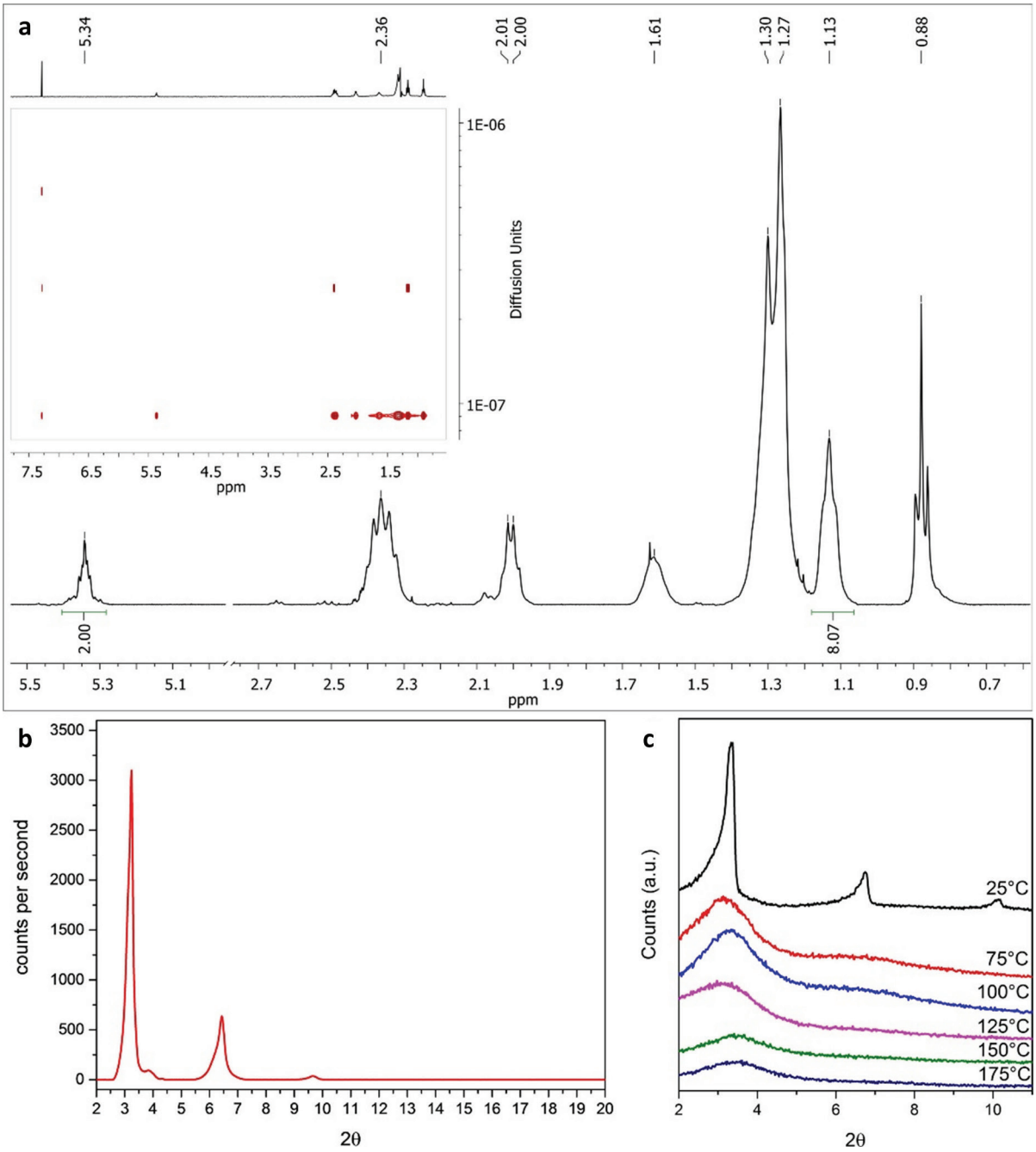

Supplementary Figure 4 | Analysis of the product obtained when propionic acid is added to Cd(oleate)$_2$ in absence of Se. **a**, ^{1}H-NMR spectrum (400 MHz, $CDCl_3$). The integral ratio of the olefinic protons (oleate moiety: m, δ = 5.34 ppm) and the methyl protons (of the propionate CH_3 terminus, t, δ = 1.13 ppm) suggest a composition close to Cd(oleate)$_{0.75}$(propionate)$_{1.25}$. However, diffusion-ordered ^{1}H-NMR spectroscopy (inset) revealed that a mixture of Cd(oleate)$_1$(propionate)$_1$ and a minor fraction of Cd(propionate)$_2$ was present. **b**, The corresponding X-ray diffraction (XRD) pattern revealed the layered structure of this material, exhibiting clear [001], [002], and [003] reflections. **c**, When heated in a nitrogen atmosphere, the layered structure is lost already at relatively low temperatures.

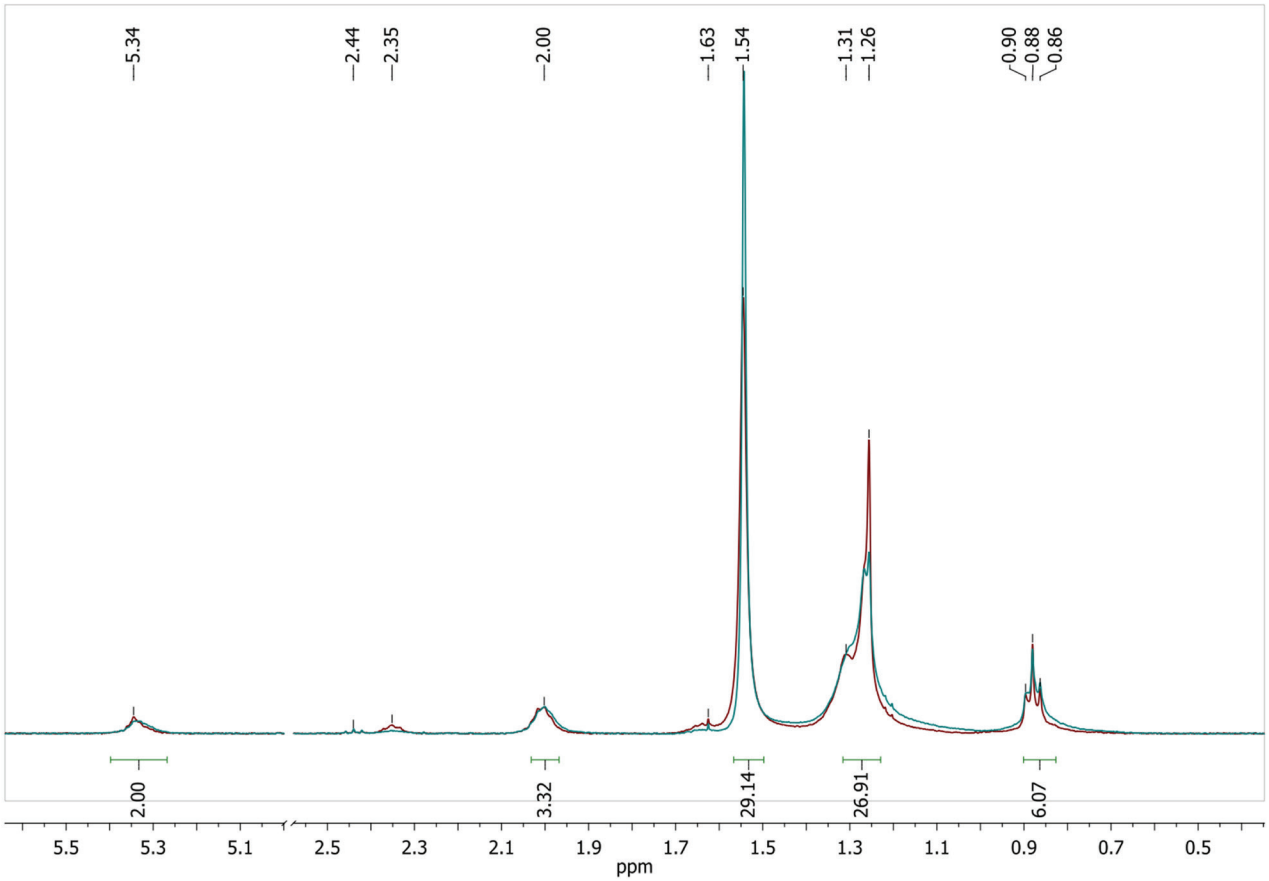

Supplementary Figure 5 | Analysis of the product obtained when butyric acid is added to Cd(oleate)$_2$ in absence of Se. ^{1}H-NMR (400 MHz) spectra of the product obtained with butyric acid (red curve) and pure Cd(oleate)$_2$ (blue curve) show that the oleate is not efficiently exchanged with butyrate since no clear signal stemming from butyrate protons could be detected.

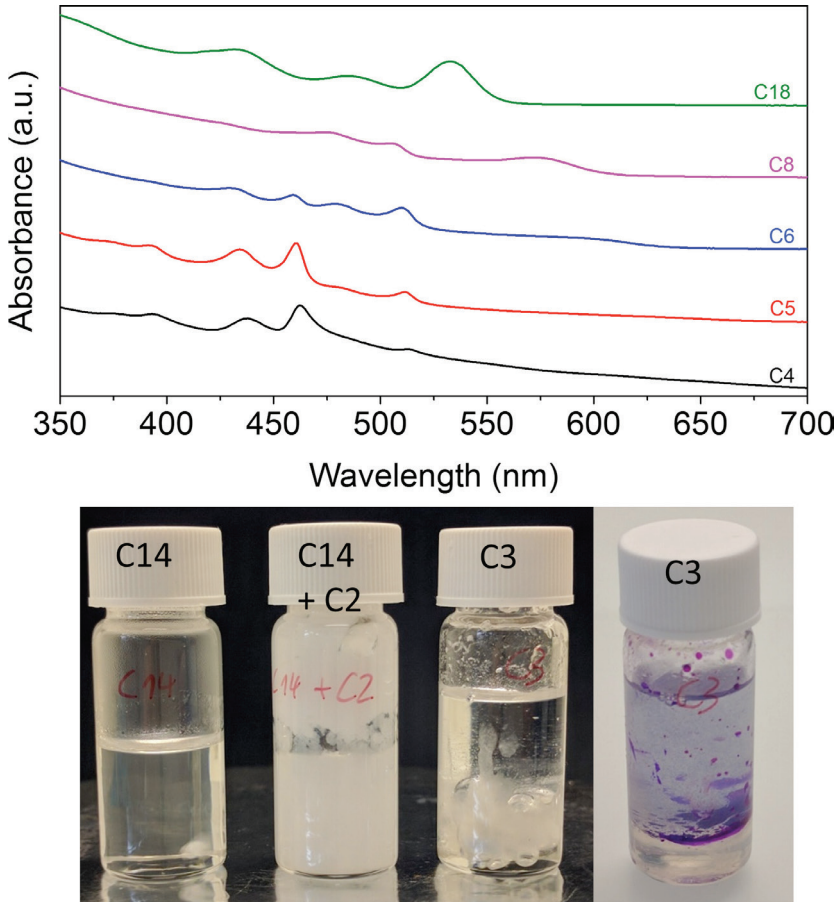

Supplementary Figure 6 | Solubility of Cd(carboxylate)$_2$ in 1-octadecene determines NPL formation. A series of Cd(carboxylates)$_2$ of different chain length (C18 = oleate, C8 = octanoate, C6 = hexanoate, C5 = pentanoate, and C4 = butanoate) were heated with elemental Se in 1-octadecene (ODE) at 180 °C. With decreasing carboxylate chain length, the amount of NPLs synthesized was found to increase. Cd(oleate)$_2$ was completely soluble and yielded only colloidal quantum dots (QDs), Cd(octanoate)$_2$ and Cd(hexanoate)$_2$ were just slightly soluble and yielded NPLs and QDs, and Cd(pentanoate)$_2$ and Cd(butanoate)$_2$ were completely insoluble and yielded only NPLs. The photographs at the bottom illustrate the solubility of various Cd(carboxylates)$_2$ in ODE. Cd(myristate)$_2$ (C14) dissolves completely in ODE at 180 °C. A 1:1 mixture of Cd(myristate)$_2$ and Cd(acetate)$_2$ (C14+C2) does not dissolve in ODE at 180 °C. The addition of Cd(acetate)$_2$ to a solution of Cd(myristate)$_2$ results in mixed Cd(carboxylates)$_2$ of the type Cd(myristate)(acetate), which phase separates from the solvent. Short-chain Cd(carboxylates)$_2$, *e.g.*, Cd (propionate)$_2$ (C3), do not dissolve in ODE and at 180 °C two immiscible liquid phases [top ODE, bottom Cd(propionate)$_2$ melt] are obtained. In the bottom right image, a dye was added to the mixture to visualize the phase separation. The NPLs shown in Fig. 1a (main text) were isolated from such phase-separated Cd(propionate)$_2$ melts.

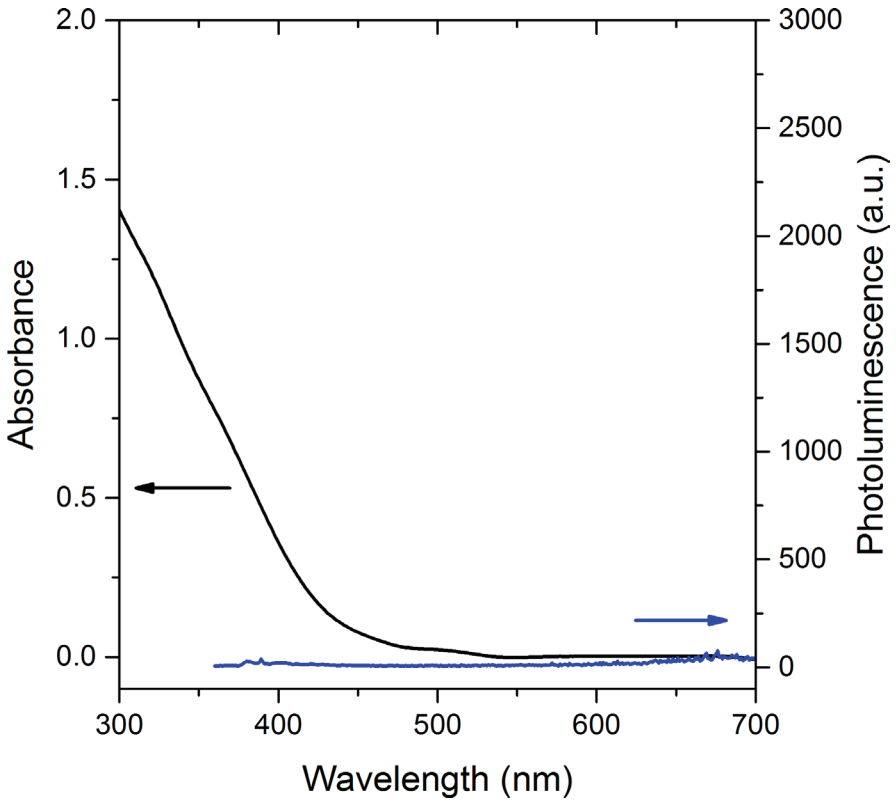

Supplementary Figure 7 | Absorption and photoluminescence spectra of the reaction solution of Cd(propionate)$_2$/Se/octadecene synthesis shown in Fig. 1a of main text. 200 mg Cd(propionate)$_2$ was mixed with 90 mL 1-octadecene (ODE) in a 250 mL three-neck flask, degassed at room temperature for 20 min, and subsequently heated to 200 °C under N_2 with magnetic stirring. At this stage, Cd(propionate)$_2$ was fully molten and present as clearly visible droplets. 72 mg Se was dispersed in 2 mL degassed ODE and injected into the reaction mixture, which was held at 200 °C for 60 min. Upon cooling to room temperature, the Cd(propionate)$_2$ droplets solidified and attached to the flask wall. The 3-monolayer-thick CdSe NPLs shown in Fig. 1a of the main text were extracted from the solidified Cd(propionate)$_2$ melt. As shown in the plot above, the absorption (quartz cuvette, 1 mm pass length) and photoluminescence spectra (excitation at 350 nm) of the undiluted, crude reaction solution did not display any features of CdSe NPLs. This indicates that the NPLs did not from in the solution, but in the melt of Cd(carboxylates)$_2$.

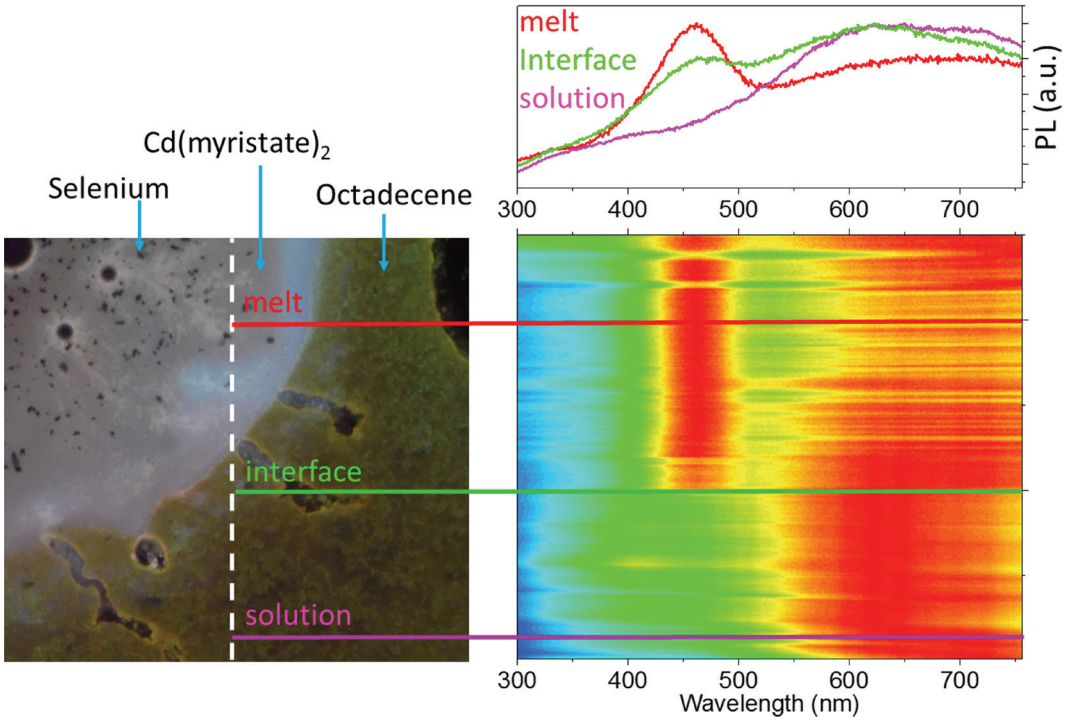

Supplementary Figure 8 | Fluorescence microscopy of Cd(myristate)$_2$/Se melts and 1-octadecene (ODE) on a microscope slide. A portion of blended Cd(myristate)$_2$/Se powder (molar ratio 3:1) and a drop of ODE were placed close together on a glass microscope slide and covered with a glass cover slip. The sample was placed on a hot plate at 180 °C for 10 min. Due to the absence of mixing, Cd(myristate)$_2$ only melted and did not dissolve completely into the ODE within the time span of the experiment. The sample was analyzed by fluorescence microscopy to obtain spatial information about the point of formation of the CdSe NPLs. The bright-field microscopy image (left panel) was recorded using a Nikon D3200 digital camera (white balance 3500 K) coupled to an inverted Nikon TiU microscope using a 2x (0.06 numerical aperture) objective under bright-field illumination. The field of view of the image is 0.51 mm in height. The image was projected onto the entrance slit of an imaging spectrograph (Princeton Instruments, Acton SP2358) under blue illumination at 385 nm (light-emitting diode) and dispersed using a 150 gr/mm grating. The resulting spectra along the line trace (white vertical line in the bright-field image) were recorded using a CCD camera (PIXIS 256E). The spatio-spectral information obtained from this experiment reveals that 3-monolayer NPLs (peak at 460 nm) are formed exclusively in the Cd(myristate)$_2$/Se melt (see red spectrum above the spatio-spectral map). At the interface between this melt and the solvent (ODE), the signal of 3-monolayer NPLs (peak at 460 nm) rapidly vanishes (green spectrum) and is completely absent in the solution (magenta spectrum). Hence, in solution, polydisperse quantum dots (QDs) are formed by classical diffusion-limited growth giving rise to the broad peak around 600 nm while non-diffusion-limited growth in the melt yields CdSe NPLs.

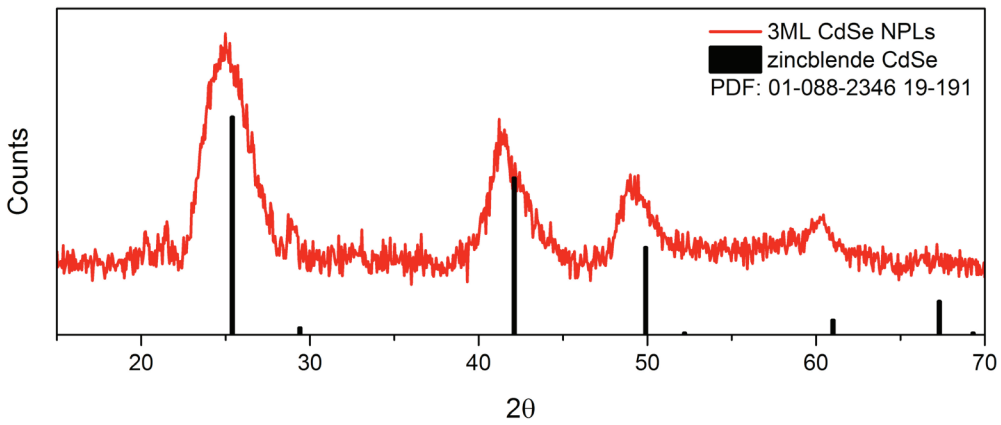

Supplementary Figure 9 | X-ray diffraction (XRD) analysis of 3-monolayer NPLs from a typical solvent-free synthesis. The obtained diffraction pattern could be indexed to zincblende CdSe with small shifts towards lower angles, indicating a slightly larger unit cell.

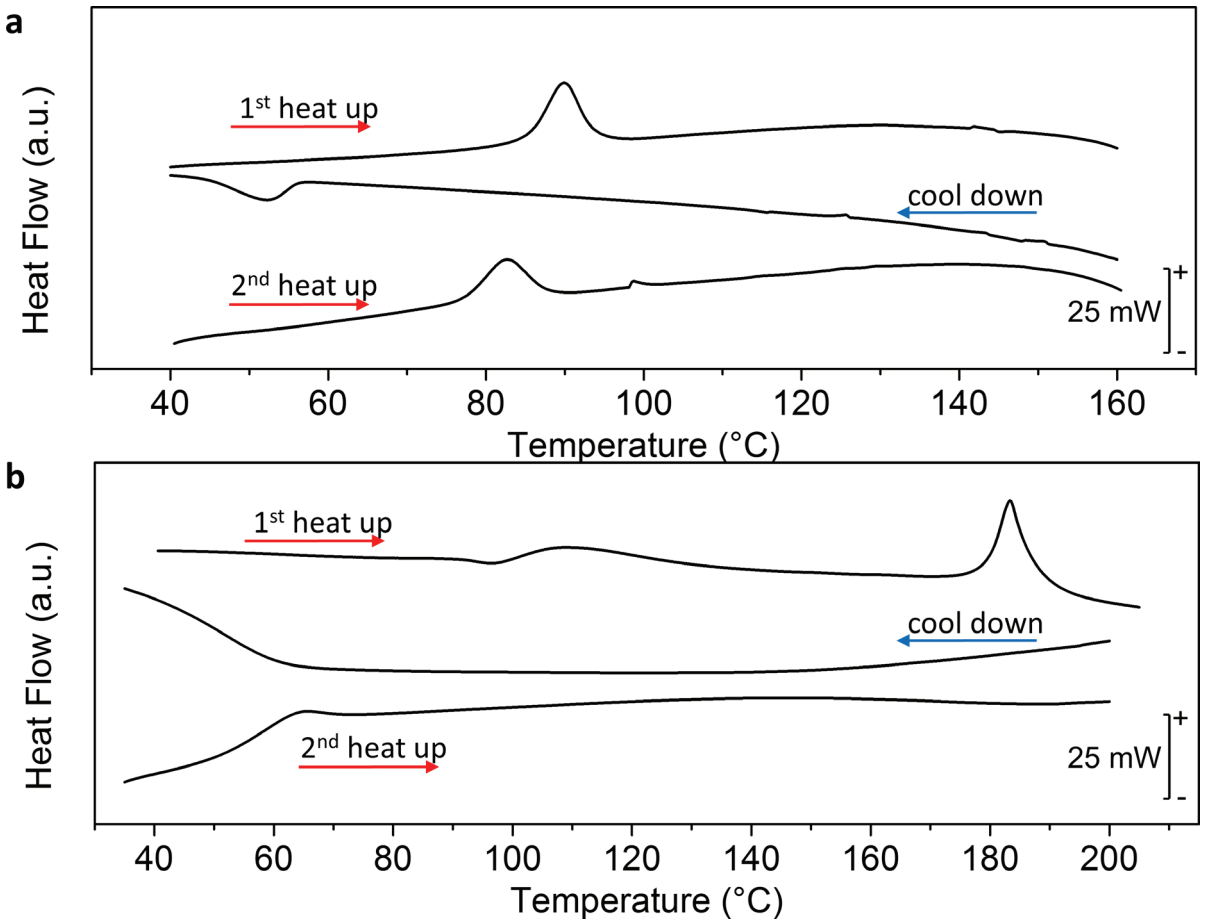

Supplementary Figure 10 | Differential scanning calorimetry (DSC) of Cd(myristate)$_2$ and Cd(propionate)$_2$ recorded at a heating/cooling rate of 10 K/min under N_2. **a**, Cd(myristate)$_2$ melted at 87 °C and recrystallized at 52 °C upon cooling. The melting temperature in the second heating step decreased to 82 °C. In contrast to Cd(propionate)$_2$, melting and crystallization are reversible for Cd(myristate)$_2$. **b**, Cd(propionate)$_2$ underwent a polymorphic transition at 110 °C and melted at 180 °C. The system did not recrystallize when cooled down, and amorphous Cd(propionate)$_2$ was obtained.

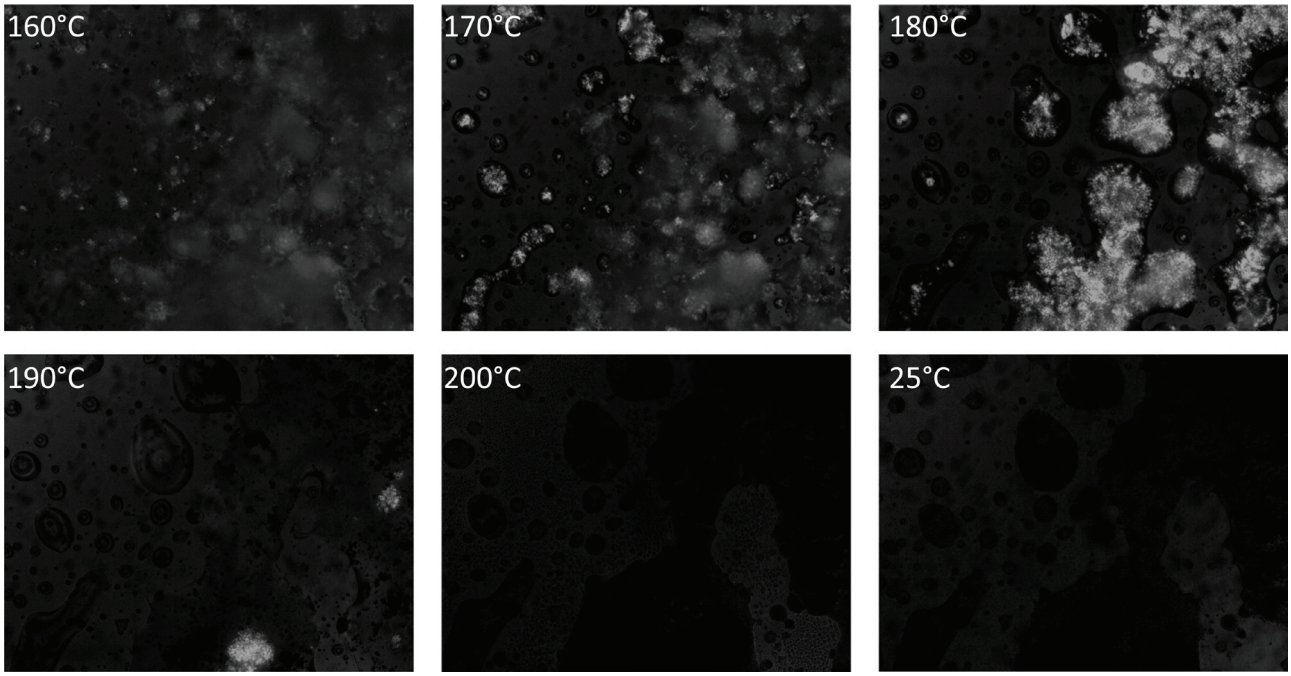

Supplementary Figure 11 | Polarized optical microscopy (POM) of Cd(propionate)$_2$/Se melts. A blend of Cd(propionate)$_2$ and Se powders (3:1 molar ratio) was heated at a rate of 10 K/min (25-200 °C) under N_2 and images were taken at different temperatures. From room temperature up to 160 °C, the sample was optically thick and very little light intensity stemming from the birefringence of the crystalline powders was observed. More signal could be detected when the material started to melt (around 170-190 °C). The birefringence detected at this point was attributed to small crystalline fragments floating in the melt of Cd(propionate)$_2$. Once a homogeneous melt was obtained (200 °C), no birefringence was observed, which was also the case after the sample was cooled back to room temperature.

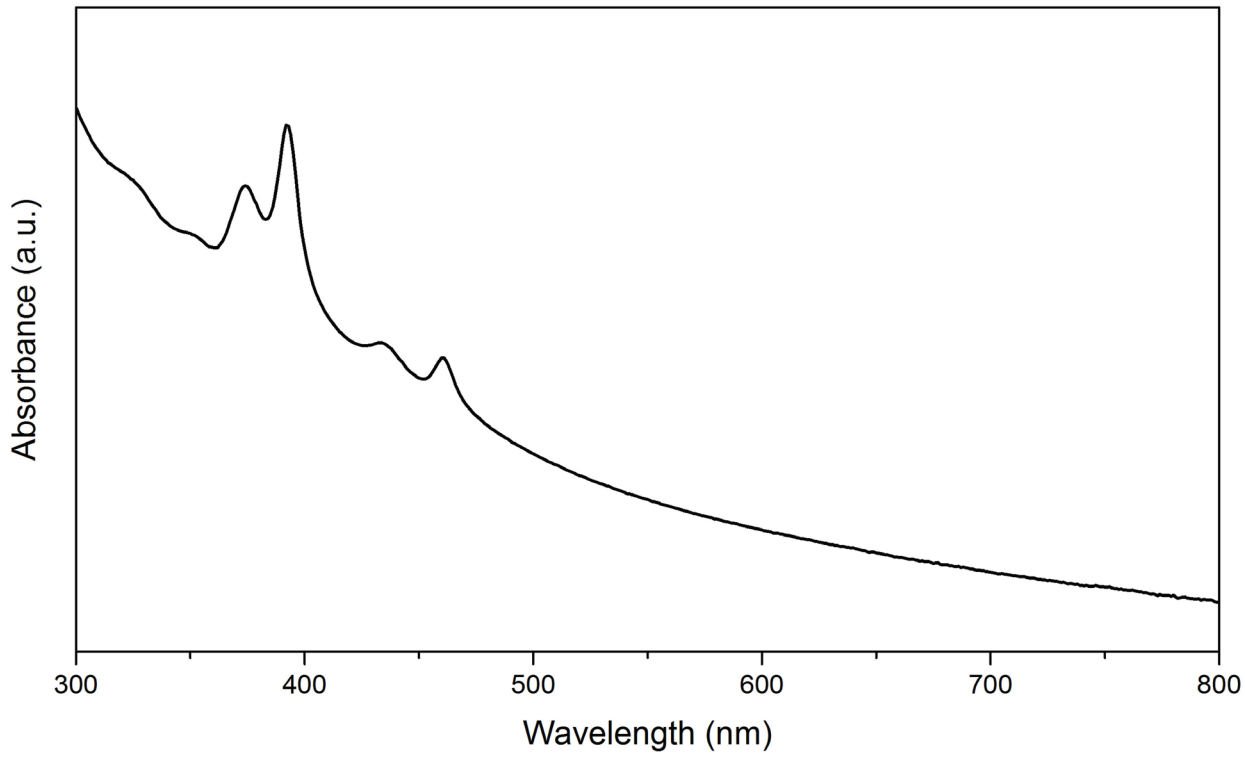

Supplementary Figure 12 | Absorption spectrum of CdSe NPLs synthesized with amorphous Cd(propionate)$_2$. Amorphous Cd(propionate)$_2$ was obtained by thermal pre-treatment (see main text and Supplementary Fig. 10), mixed with elemental Se and reacted at 200 °C for 4 h. Absorption features of 2-monolayer (372 and 393 nm) and 3-monolayer (435 and 461 nm) zincblende CdSe NPLs can be observed. The fact that NPLs could form from amorphous precursors proves conclusively that NPLs form in a completely isotropic environment.

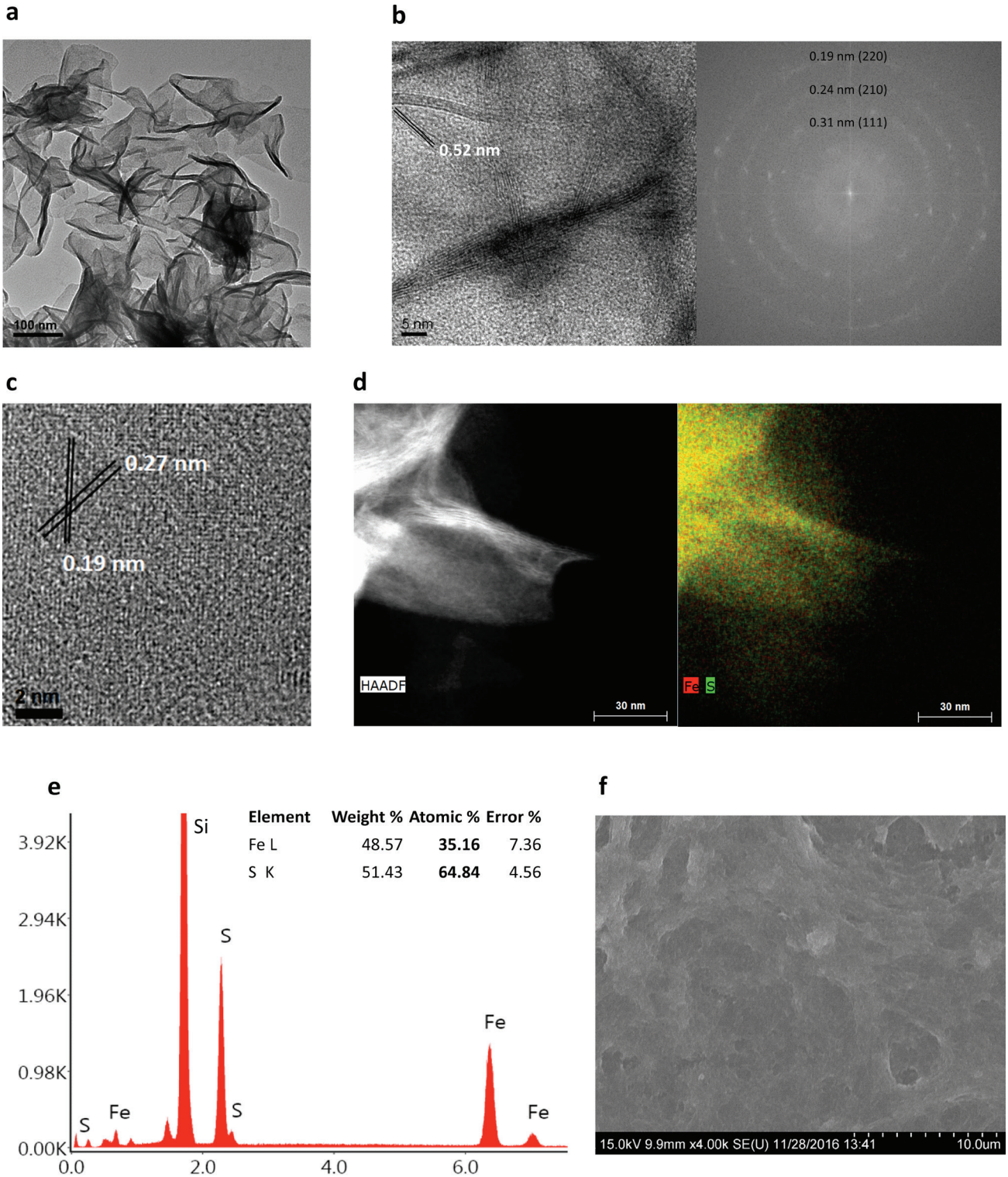
a
100 nm
b
0.52 nm
5 nm
0.19 nm (220)
0.24 nm (210)
0.31 nm (111)
c
0.27 nm
0.19 nm
2 nm
d
HAADF
30 nm
Fe S
30 nm
e
Element Weight % Atomic % Error %
Fe L 48.57 35.16 7.36
S K 51.43 64.84 4.56
3.92K
2.94K
1.96K
0.98K
0.00K
0.0
2.0
4.0
6.0
Si
S
Fe
S
S
Fe
Fe
f
15.0kV 9.9mm x4.00k SE(U) 11/28/2016 13:41
10.0um

Supplementary Figure 13 | Analysis of pyrite-FeS_2 NPLs. a, Low-resolution transmission electron micrograph (TEM) of the obtained NPLs (see Methods for synthesis details). The resulting NPLs are up to several 100 nm wide and typically form rolled up and twisted agglomerates. **b**, High-resolution TEM and corresponding Fourier transform of an agglomerated region. We observe lattice distances that are in good agreement with the cubic FeS_2 phase (pyrite, pdf 6-710). In addition, we observe stack-like structures with a characteristic distance of 0.52 nm, from which we estimate the NPL thickness to be less than 3 monolayers (corresponding to one unit cell = 0.54 nm). **c**, High-resolution TEM of a NPL lying flat on the grid. We observe the characteristic lattice distances for the (220) and the (200) planes of pyrite. We note that for a single monolayer of pyrite, we would not expect to see the former. Thus, our data suggests that we synthesized 2 monolayer pyrite FeS_2 NPLs. **d**, Scanning transmission electron micrograph (STEM) and corresponding energy-dispersive X-ray spectroscopy (EDS) map, which clearly demonstrate homogeneously distributed iron and sulfur throughout the NPLs. **e**, EDS spectrum of a drop-casted, thick film of pyrite FeS_2 NPLs. We measured a Fe:S ratio of 1:1.84, in good agreement with pyrite (expected ratio 1:2). In addition, we note the absence of significant carbon signal, which is consistent with unpassivated surfaces. **f**, Scanning electron micrograph (SEM) of the same drop-casted film.

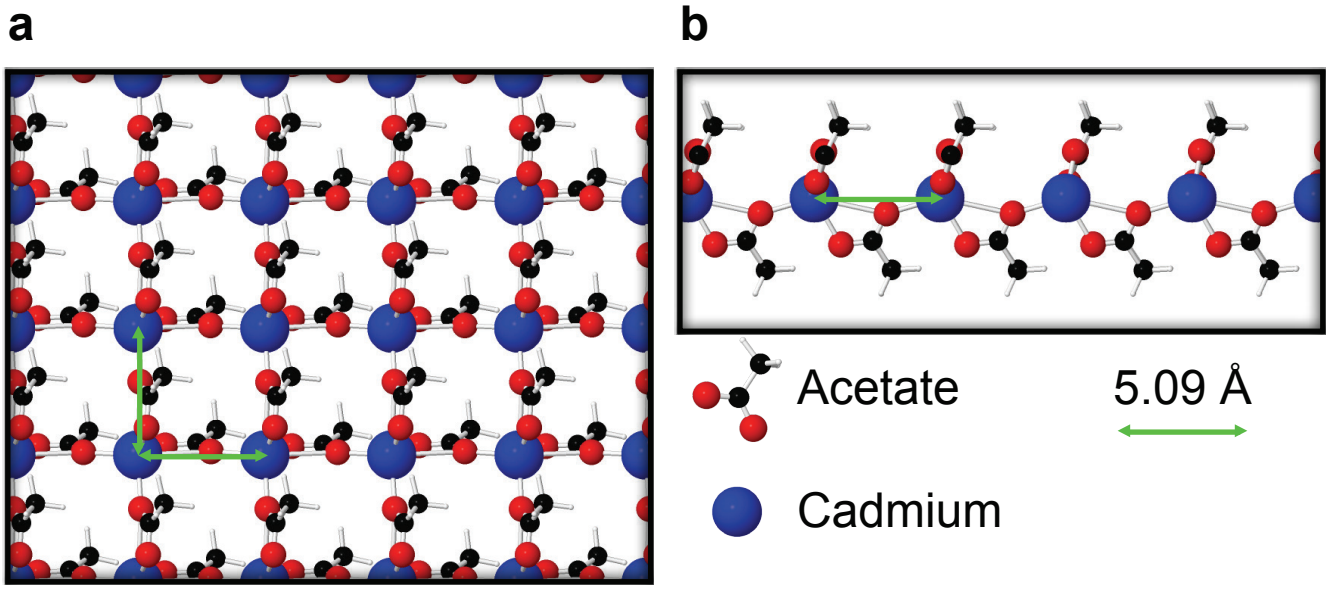

Supplementary Figure 14 | Structure of the Cd-acetate phase used for our DFT calculations. We used 2-dimensional coordination polymers of $Cd(acetate)_2$ to estimate the energy of the Cd-acetate precursor. Projections of this 2-dimensional polymer from the top and the side are shown in **a** and **b**, respectively.

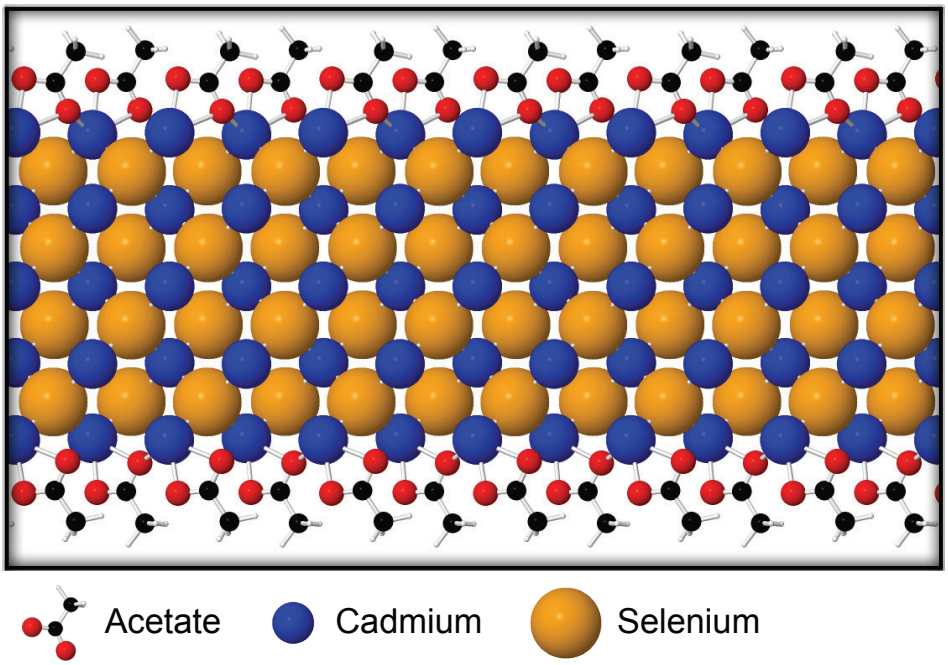

Supplementary Figure 15 | Side view of a 4-monolayer-thick CdSe(001) zincblende nanoplatelet. The {001} surfaces are Cd-terminated and passivated by acetate molecules that form bidentate bonds to the Cd atoms on the surface.

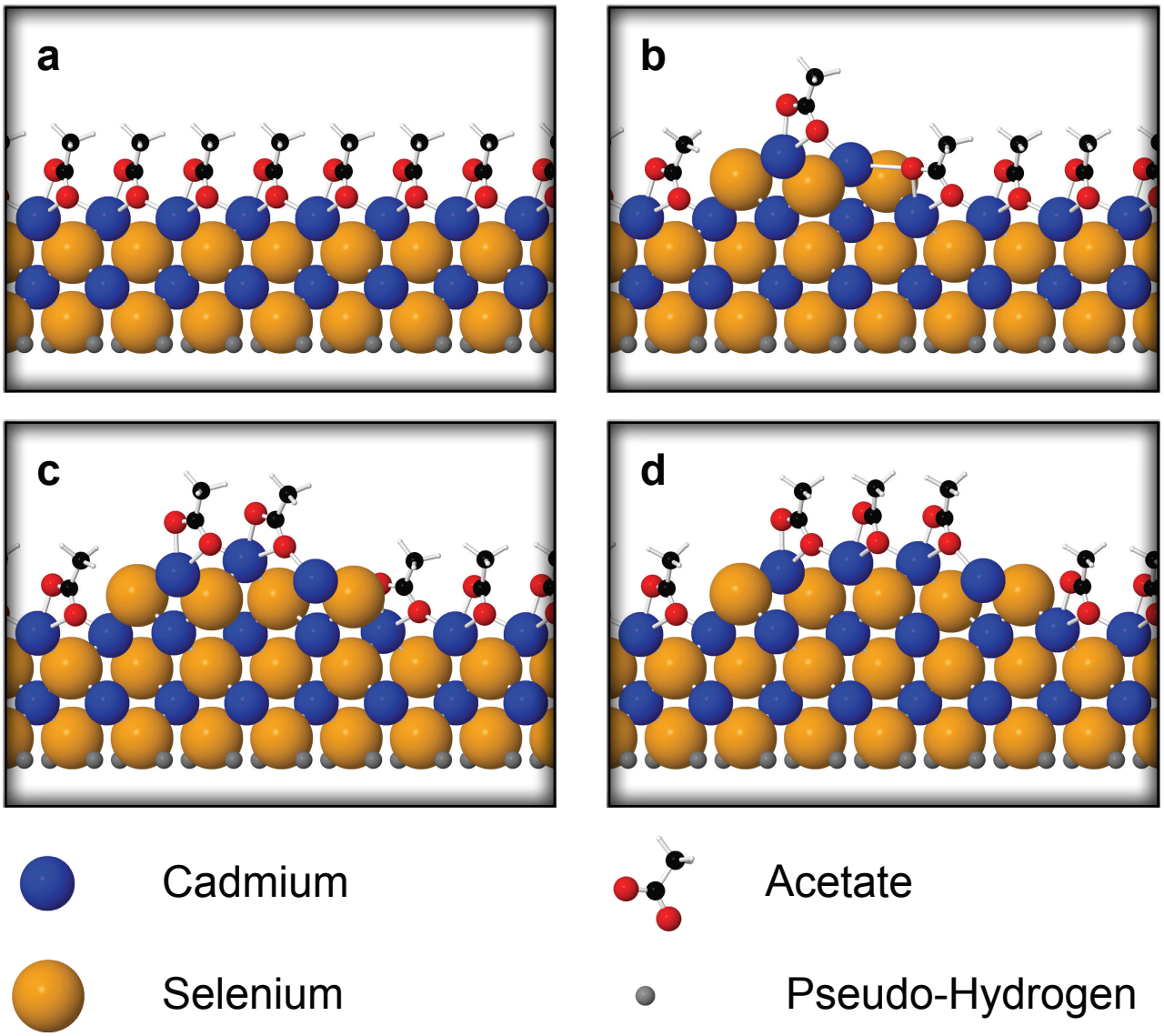

Supplementary Figure 16 | Calculation of the edge formation energy for CdSe. a, The reference geometry is a two-monolayer-thick CdSe(001) slab passivated on top by acetates and on the bottom by pseudo-hydrogen atoms. **b-d**, Different computational supercells with electronic closed-shell structures following the electron-counting rule. We obtained formation energies of 58 meV (E_L= 40 meV/Å), 42 meV (E_L= 24 meV/Å), and 65 meV (E_L= 47 meV/Å) for **b**, **c**, and **d**, respectively.

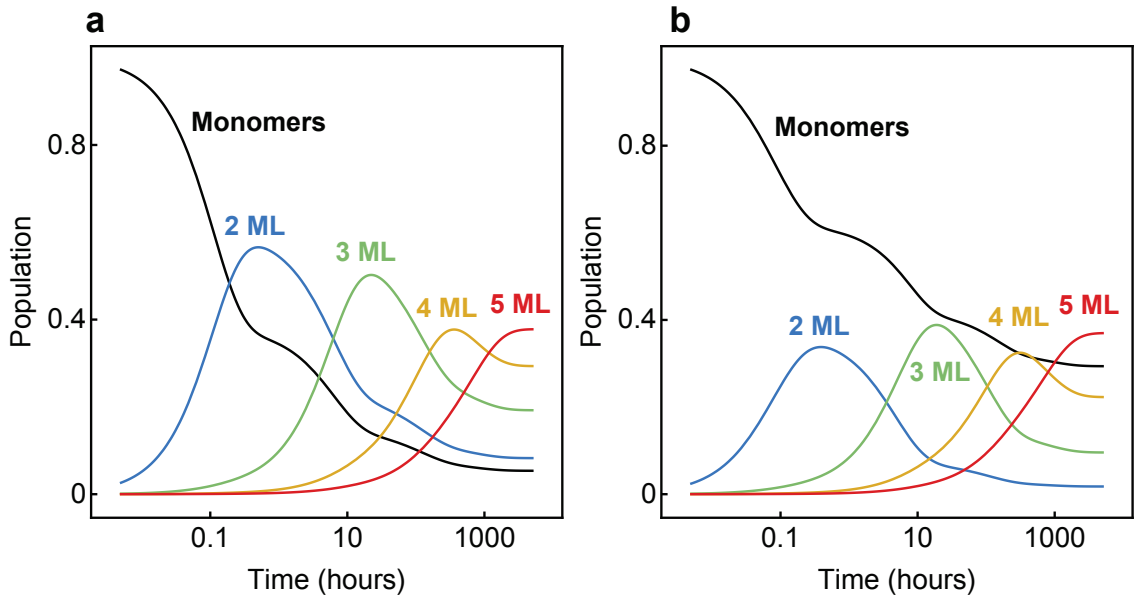

Supplementary Figure 17 | Comparison of the simplified NPL growth model based on first-order kinetics with a more realistic model including geometric considerations. **a**, Solution of the simple model at T = 200 °C with k_0 fitted to experimentally observed timescales (see Supplementary Section 1.d and the main text). The curves are labeled by the NPL thickness in monolayers (ML). **b**, More realistic model solved with the value for k_0 extracted from the first-order model.

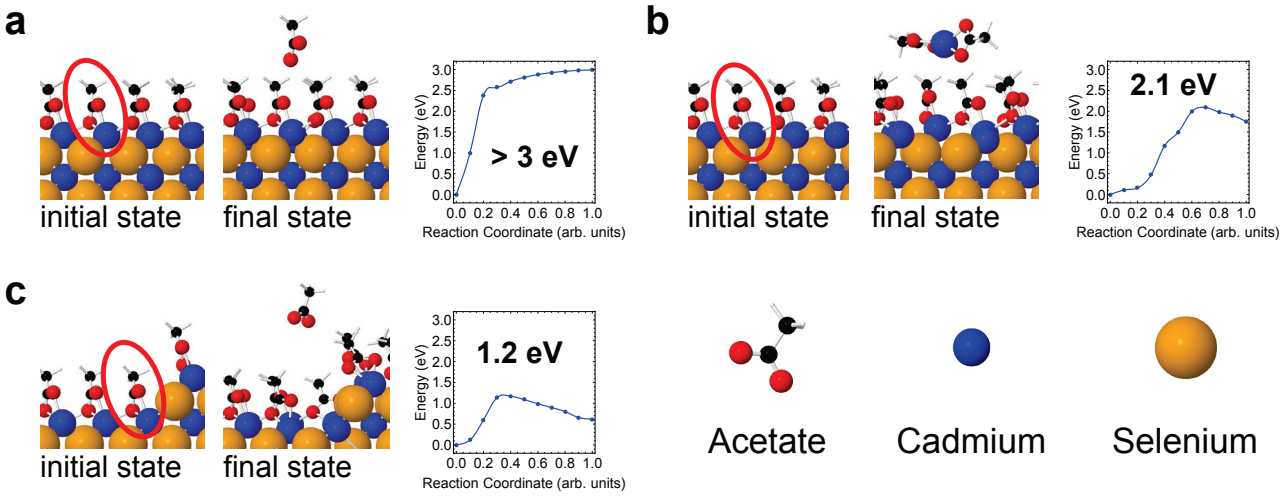

Supplementary Figure 18 | Calculation of the minimum energy path for selected surfactant desorption reactions. Desorbing molecules are marked with a red circle in the initial state. **a**, Desorption of acetate from a perfectly flat CdSe(001) surface has an energy barrier of more than 3 eV. **b**, Desorption of $Cd(acetate)_2$ from this surface has a reduced barrier of 2.1 eV. **c**, The barrier for desorption of the acetate next to a surface step is only 1.2 eV.

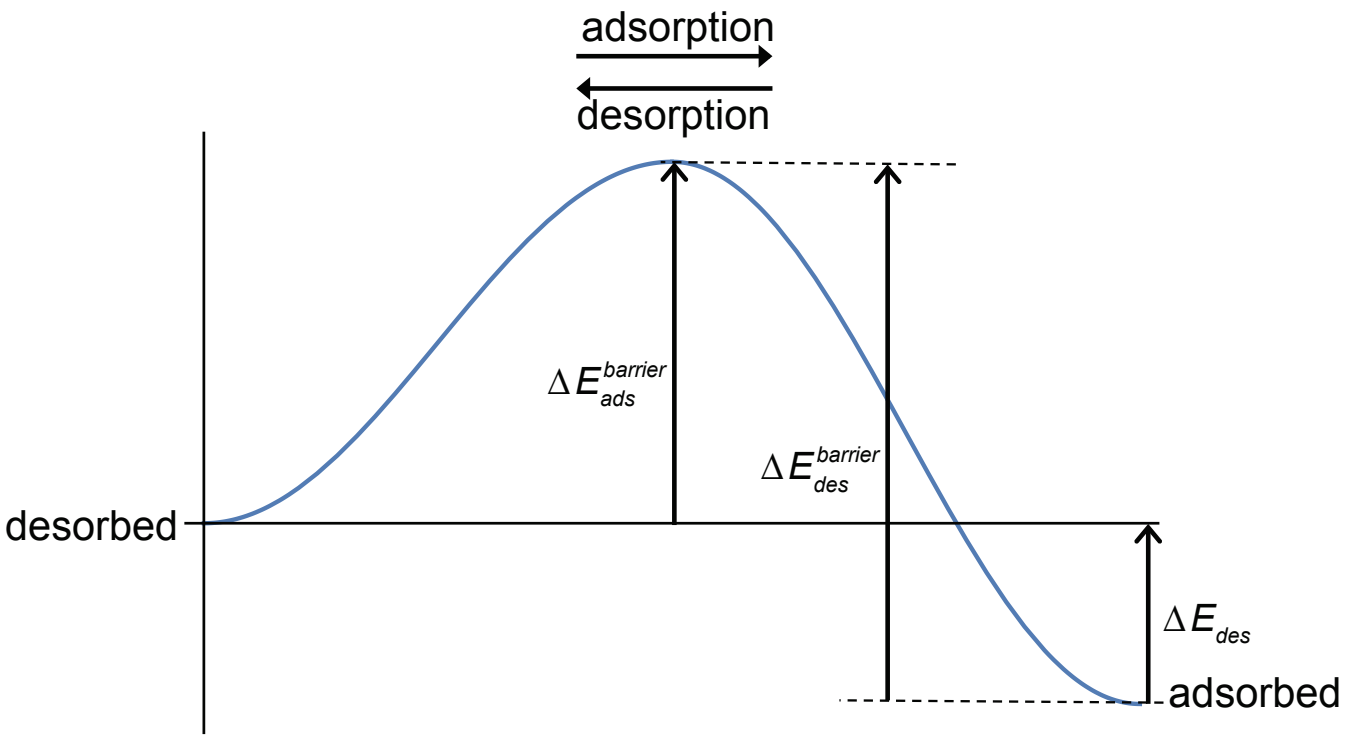

Supplementary Figure 19 | Schematic potential-energy surface for monomer adsorption and desorption reactions. The reaction coordinate going from left to right corresponds to the reaction of transferring a monomer from the melt to a crystal surface. The corresponding barrier is known from DFT calculations of surfactant desorption reactions. The reaction coordinate going from right to left is the desorption reaction for which the barrier is given by the sum of the monomer adsorption barrier and the energy difference between desorbed and adsorbed state.

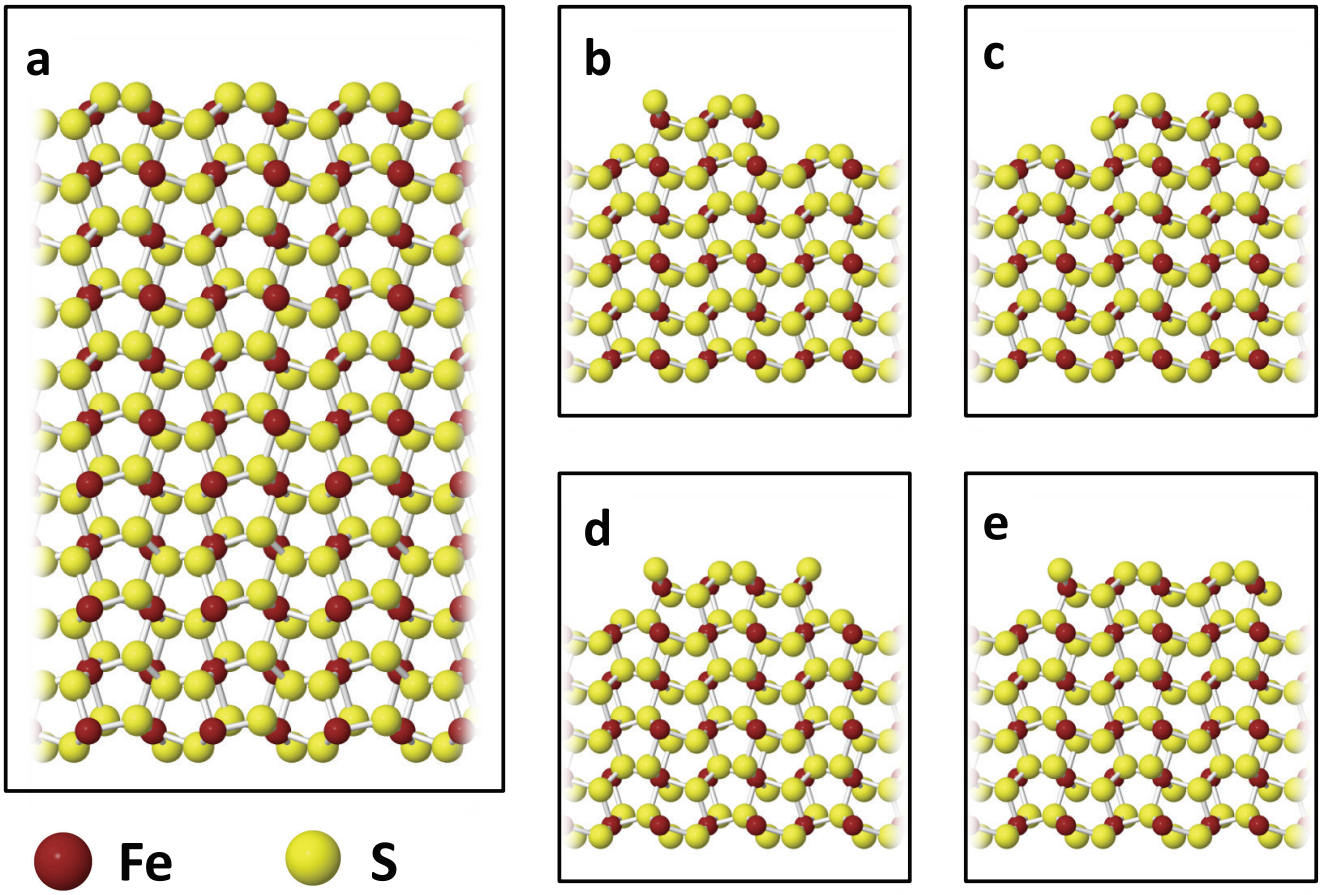

Supplementary Figure 20 | Facet and surface-island geometries of cubic FeS_2. **a**, Structure of the pyrite slab used in our DFT calculation to evaluate the surface energy of the stoichiometric (001) surface shown from the side. From this relaxed slab structure, we obtained a value of $E_A = 64$ meV/Å^2 for the surface energy. **b**–**e**, The 4 different relaxed island geometries we used to estimate the edge energy in pyrite. We found these energies to be 45 meV/Å, 52 meV/Å, 50 meV/Å, and 40 meV/Å for the structures **b**, **c**, **d**, and **e**, respectively, with an average edge energy given by $E_L = 47$ meV/Å.

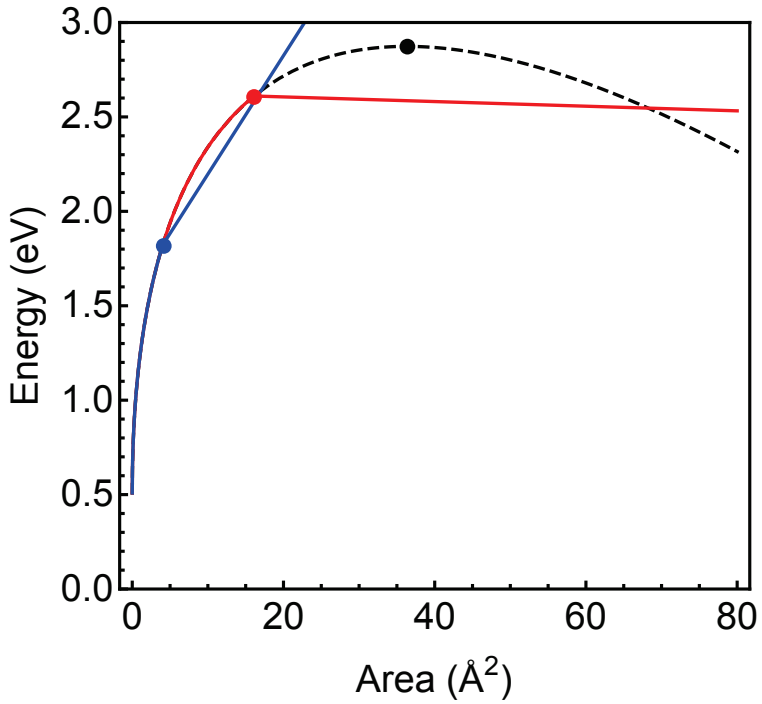

Supplementary Figure 21 | The minimum energy path of surface island nucleation and growth in cubic FeS_2. We computed these energy curves with the model parameters for cubic FeS_2 discussed in Supplementary Section 1.g. We find that only the growth of 2-monolayer-thick nanoplatelets (red curve) is kinetically favored over wide-facet growth (dashed black curve). No kinetic instabilities exist for thicker nanoplatelets. The 1-monolayer-thick platelet (blue curve) is not thermodynamically stable and therefore has no driving force to grow.

Section 3. Supplementary references

S1. Van de Walle, C. G., Laks, D. B., Neumark, G. F. & Pantelides, S. T. First-principles calculations of solubilities and doping limits: Li, Na, and N in ZnSe. *Phys. Rev. B* **47**, 9425-9434 (1993).

S2. Van de Walle, C. G. & Neugebauer, J. First-principles calculations for defects and impurities: Applications to III-nitrides. *J. Appl. Phys.* **95**, 3851-3879 (2004).

S3. Lany, S. & Zunger, A. Accurate prediction of defect properties in density functional supercell calculations. *Model. Simul. Mater. Sci. Eng.* **17**, 084002 (2009).

S4. Kuvadia, Z. B. & Doherty, M. F. Spiral growth model for faceted crystals of non-centrosymmetric organic molecules grown from solution. *Cryst. Growth Des.* **11**, 2780-2802 (2011).

S5. Lovette, M. A. & Doherty, M. F. Predictive modeling of supersaturation-dependent crystal shapes. *Cryst. Growth Des.* **12**, 656-669 (2012).

S6. Kim, S. H., Dandekar, P., Lovette, M. A. & Doherty, M. F. Kink rate model for the general case of organic molecular crystals. *Cryst. Growth Des.* **14**, 2460-2467 (2014).

S7. Ohara, M. & Reid, R. C., *Modeling Crystal Growth Rates from Solution*. (Prentice-Hall, 1973).

S8. Henkelman, G., Uberuaga, B. P. & Jónsson, H. A climbing image nudged elastic band method for finding saddle points and minimum energy paths. *J. Chem. Phys.* **113**, 9901-9904 (2000).

S9. Hung, A., Muscat, J., Yarovsky, I. & Russo, S. P. Density-functional theory studies of pyrite FeS_2(100) and (110) surfaces. *Surf. Sci.* **513**, 511-524 (2002).

Section 4. Supplementary movies

Supplementary Movie 1 | A kinetic Monte Carlo (kMC) simulation of CdSe crystal growth at 650 K. The animation shows how new monomers (light blue spheres) attach and detach on a crystal with rates given by Eq. (S37). The initial crystal consists of a single monomer (orange sphere). Through the random attachment of monomers, a slightly asymmetric crystallite forms with a strongly increased growth barrier on its wider facets. Subsequently, a highly anisotropic nanoplatelet evolves that does not grow in thickness.

Supplementary Movie 2 | A kinetic Monte Carlo (kMC) simulation of CdSe crystal growth at 1500 K. Like in Supplementary Movie 1, an initial monomer (orange ball) grows via the attachment and detachment of new monomers (light blue balls) according to Eq. (S37). However, due to the high thermal energy available at 1500 K, the kinetic instabilities that would cause anisotropic growth of nanoplatelets are not relevant. Under such conditions, isotropic growth is observed leading to roughly cubic crystal shapes.